

Analysis of Polarized Dust Emission Using Data from the First Flight of SPIDER

SPIDER COLLABORATION, P. A. R. ADE,¹ M. AMIRI,² S. J. BENTON,³ A. S. BERGMAN,³ R. BIHARY,⁴ J. J. BOCK,^{5,6} J. R. BOND,⁷ J. A. BONETTI,⁶ S. A. BRYAN,⁸ H. C. CHIANG,^{9,10} C. R. CONTALDI,¹¹ O. DORÉ,^{5,6} A. J. DUIVENVOORDEN,^{12,3} H. K. ERIKSEN,¹³ J. P. FILIPPINI,¹⁴ A. A. FRAISSE,³ K. FREESE,^{15,16,17} M. GALLOWAY,¹³ A. E. GAMBREL,¹⁸ N. N. GANDILO,¹⁹ K. GANGA,²⁰ S. GOURAPURA,³ R. GUALTIERI,^{14,21} J. E. GUDMUNDSSON,^{22,17} M. HALPERN,² J. HARTLEY,²³ M. HASSELFIELD,²⁴ G. HILTON,²⁵ W. HOLMES,⁶ V. V. HRISTOV,⁵ Z. HUANG,⁷ K. D. IRWIN,^{26,27} W. C. JONES,³ A. KARAKCI,¹³ C. L. KUO,²⁶ Z. D. KERMISH,³ J. S.-Y. LEUNG,^{28,29} S. LI,^{3,30} D. S. Y. MAK,¹¹ P. V. MASON,⁵ K. MEGERIAN,⁶ L. MONCELSI,⁵ T. A. MORFORD,⁵ J. M. NAGY,⁴ C. B. NETTERFIELD,^{28,23} M. NOLTA,⁷ R. O'BRIENT,⁶ B. OSHERSON,¹⁴ I. L. PADILLA,^{4,28,31} B. RACINE,¹³ A. S. RAHLIN,^{32,18} C. REINTSEMA,²⁵ J. E. RUHL,⁴ M. C. RUNYAN,⁵ T. M. RUUD,¹³ J. A. SHARIFF,⁷ E. C. SHAW,^{14,15,16} C. SHIU,³ J. D. SOLER,³³ X. SONG,³ A. TRANGSRUD,^{5,6} C. TUCKER,¹ R. S. TUCKER,⁵ A. D. TURNER,⁶ J. F. VAN DER LIST,³ A. C. WEBER,⁶ I. K. WEHUS,¹³ D. V. WIEBE,² AND E. Y. YOUNG^{26,27}

¹*School of Physics and Astronomy, Cardiff University, The Parade, Cardiff, CF24 3AA, UK*

²*Department of Physics and Astronomy, University of British Columbia, 6224 Agricultural Road, Vancouver, BC V6T 1Z1, Canada*

³*Department of Physics, Princeton University, Jadwin Hall, Princeton, NJ 08544, USA*

⁴*Physics Department, Case Western Reserve University, 10900 Euclid Ave, Rockefeller Building, Cleveland, OH 44106, USA*

⁵*Division of Physics, Mathematics and Astronomy, California Institute of Technology, MS 367-17, 1200 E. California Blvd., Pasadena, CA 91125, USA*

⁶*Jet Propulsion Laboratory, Pasadena, CA 91109, USA*

⁷*Canadian Institute for Theoretical Astrophysics, University of Toronto, 60 St. George Street, Toronto, ON M5S 3H8, Canada*

⁸*School Of Earth and Space Exploration, Arizona State University, 650 E Tyler Mall, Tempe, AZ 85281, USA*

⁹*Department of Physics, McGill University, 3600 Rue University, Montreal, QC, H3A 2T8, Canada*

¹⁰*School of Mathematics, Statistics and Computer Science, University of KwaZulu-Natal, Durban, South Africa*

¹¹*Blackett Laboratory, Imperial College London, SW7 2AZ, London, UK*

¹²*Center for Computational Astrophysics, Flatiron Institute, New York, NY 10010, USA*

¹³*Institute of Theoretical Astrophysics, University of Oslo, P.O. Box 1029 Blindern, NO-0315 Oslo, Norway*

¹⁴*Department of Physics, University of Illinois Urbana-Champaign, 1110 W. Green Street, Urbana, IL 61801, USA*

¹⁵*Department of Physics, University of Texas, 2515 Speedway, C1600, Austin, TX 78712, USA*

¹⁶*Weinberg Institute for Theoretical Physics, Texas Center for Cosmology and Astroparticle Physics, Austin, TX 78712, USA*

¹⁷*The Oskar Klein Centre for Cosmoparticle Physics, Department of Physics, Stockholm University, AlbaNova, SE-106 91 Stockholm, Sweden*

¹⁸*Kavli Institute for Cosmological Physics, University of Chicago, 5640 S Ellis Avenue, Chicago, IL 60637 USA*

¹⁹*Steward Observatory, 933 North Cherry Avenue, Tucson, AZ, 85721, USA*

²⁰*APC, Univ. Paris Diderot, CNRS/IN2P3, CEA/Irfu, Obs de Paris, Sorbonne Paris Cité, France*

²¹*Department of Physics & Astronomy, Northwestern University, Evanston, IL 60208, USA*

²²*Science Institute, University of Iceland, 107 Reykjavik, Iceland*

²³*Department of Physics, University of Toronto, 60 St George Street, Toronto, ON M5S 3H4 Canada*

²⁴*Department of Astronomy and Astrophysics, Pennsylvania State University, 520 Davey Lab, University Park, PA 16802, USA*

²⁵*National Institute of Standards and Technology, 325 Broadway Mailcode 817.03, Boulder, CO 80305, USA*

²⁶*Department of Physics, Stanford University, 382 Via Pueblo Mall, Stanford, CA 94305, USA*

²⁷*SLAC National Accelerator Laboratory, 2575 Sand Hill Road, Menlo Park, CA 94025, USA*

²⁸*Department of Astronomy and Astrophysics, University of Toronto, 50 St George Street, Toronto, ON M5S 3H4 Canada*

²⁹*Dunlap Institute for Astronomy and Astrophysics, University of Toronto, 50 St George Street, Toronto, ON M5S 3H4 Canada*

³⁰*Department of Mechanical and Aerospace Engineering, Princeton University, Engineering Quadrangle, Princeton, NJ 08544, USA*

³¹*Department of Physics and Astronomy, Johns Hopkins University, 3701 San Martin Drive, Baltimore, MD 21218 USA*

³²*Department of Astronomy and Astrophysics, University of Chicago, 5640 S Ellis Avenue, Chicago, IL 60637 USA*

³³*Max-Planck-Institute for Astronomy, Konigstuhl 17, 69117, Heidelberg, Germany*

ABSTRACT

Corresponding author: Jeffrey P. Filippini
jpf@illinois.edu

Using data from the first flight of SPIDER and from *Planck* HFI, we probe the properties of polarized emission from interstellar dust in the SPIDER observing region. Component separation algorithms operating in both the spatial and harmonic domains are applied to probe their consistency and to quantify modeling errors associated with their assumptions. Analyses spanning the full SPIDER region demonstrate that *i*) the spectral energy distribution of diffuse Galactic dust emission is broadly consistent with a modified-blackbody (MBB) model with a spectral index of $\beta_d = 1.45 \pm 0.05$ (1.47 ± 0.06) for *E* (*B*)-mode polarization, slightly lower than that reported by *Planck* for the full sky; *ii*) its angular power spectrum is broadly consistent with a power law; and *iii*) there is no significant detection of line-of-sight decorrelation of the astrophysical polarization. The size of the SPIDER region further allows for a statistically meaningful analysis of the variation in foreground properties within it. Assuming a fixed dust temperature $T_d = 19.6$ K, an analysis of two independent sub-regions of that field results in inferred values of $\beta_d = 1.52 \pm 0.06$ and $\beta_d = 1.09 \pm 0.09$, which are inconsistent at the 3.9σ level. Furthermore, a joint analysis of SPIDER and *Planck* 217 and 353 GHz data within a subset of the SPIDER region is inconsistent with a simple MBB at more than 3σ , assuming a common morphology of polarized dust emission over the full range of frequencies. These modeling uncertainties have a small—but non-negligible—impact on limits on the cosmological tensor-to-scalar ratio derived from the SPIDER dataset. The fidelity of the component separation approaches of future CMB polarization experiments may thus have a significant impact on their constraining power.

1. INTRODUCTION

The polarization of the cosmic microwave background (CMB) contains a wealth of information about the contents, history, and origins of the Universe (Abazajian et al. 2016). Observations of the *E*-mode (“gradient”, scalar, even-parity) polarization pattern reveal details of acoustic oscillations in the primordial plasma. A measurement of a cosmological *B*-mode (“curl”, pseudoscalar, odd-parity) pattern on large angular scales would imply the presence of a background of primordial gravitational waves, and thus provide remarkable new insights into early Universe models (Kamionkowski & Kovetz 2016; Seljak & Zaldarriaga 1997).

Precision studies of CMB polarization are complicated by polarized emission at similar frequencies from foreground sources within our own Galaxy, notably synchrotron radiation and thermal emission from dust particles (Dunkley et al. 2009). Even at the highest Galactic latitudes, foreground emission is known to be far brighter than any primordial *B*-mode signal (BICEP2/Keck, Planck Collaborations et al. 2015). Observations at multiple frequencies can be used to differentiate CMB from foreground emission based upon their differing spectral energy distributions (SEDs) (Wright et al. 1991; Brandt et al. 1994). Several such component separation methods have been developed: see, e.g., Planck Collaboration et al. (2020a) and references therein. In order to stitch together such multi-frequency data, these methods must necessarily make assumptions about the nature of foregrounds: their spatial morphology, SED, or some combination thereof. Component separation is thus an imperfect process, and there are always some uncertainties due to these assumptions (Remazeilles et al. 2016; Hensley & Bull 2018).

At frequencies above 100 GHz, Galactic dust emission is the dominant polarized foreground on large angular scales (Planck Collaboration 2016). Dust grains, heated by stellar radiation to ~ 20 K, thermally re-emit that energy with

an efficiency that depends on the physical characteristics of the grains. Because emission is inefficient at wavelengths much larger than the grain itself, dust emissivity is expected to drop in the *mm*-wave regime where CMB measurements occur (Draine & Fraisse 2009). Aspherical grains that are ferro- or para-magnetic will preferentially align relative to the local magnetic field, leading to linearly-polarized emission with large-scale correlations (Purcell 1975). Motivated by this picture, it is common to model the dust SED¹ as a thermal blackbody at temperature T_d , modified by a power-law emissivity with exponent β_d :

$$I(\nu) = \tau_0 \left(\frac{\nu}{\nu_0} \right)^{\beta_d} B(\nu, T_d). \quad (1)$$

Here B is the Planck spectrum for a blackbody emitter, ν_0 is some reference frequency, and τ_0 is the optical depth at the reference frequency. Equation 1 is referred to as a *modified blackbody* (MBB).

Though widely-used, this simple model is unlikely to reflect the full range of dust emission across the sky. The detailed nature of dust grains remains a subject of ongoing research (Hensley & Draine 2022; Draine & Fraisse 2009). Their composition, size distribution, and density are all expected to vary from place to place, as are their radiative and magnetic environments. Thus, we may naturally expect different dust populations in our Galaxy to exhibit different SEDs. Such variation of the spatial morphology of a foreground component with observation frequency—or, equivalently, of the component SED across the sky—is often called *frequency decorrelation*. Furthermore, observations of the

¹ Note that, while Equation 1 may be used to model both the intensity and polarization of dust emission, the same model parameters need not apply to both; indeed, *Planck* has found a slightly steeper power law for polarization than for intensity in an all-sky analysis Planck Collaboration et al. (2020b).

CMB constitute a collection of line-of-sight (LOS) integrals through the materials surrounding us, each of which may traverse heterogeneous populations. In addition to complicating the dust SED, such *LOS decorrelation* can yield variation in polarization angle with frequency even within a single map pixel (Tassis & Pavlidou 2015).

Decorrelation may significantly complicate efforts at component separation. For example, Poh & Dodelson (2017) have shown that naive extrapolation of dust templates made from 353 GHz data to lower frequencies can bias the recovery of the tensor-to-scalar ratio $r \leq 1.5 \times 10^{-3}$. While an analysis by the BICEP team (BICEP/Keck Collaboration et al. 2023) showed no evidence of dust decorrelation within their observing region, there is evidence for its presence in larger regions. By identifying regions of the sky likely to contain magnetically misaligned clouds, Pelgrims et al. (2021) demonstrate that LOS frequency decorrelation is detectable within the *Planck* dataset, largely in the Northern Galactic cap. Ritacco et al. (2023) has further demonstrated LOS frequency decorrelation in large-scale regions close to the Galactic plane. It is thus critically important to test the assumptions behind common foreground separation techniques through detailed studies of dust polarization. Such studies will inform both the field of Galactic astrophysics as well as the prospects for foreground removal by future CMB experiments (Hensley et al. 2022; Hazumi et al. 2020; Abazajian et al. 2016).

This publication is part of a series describing results from the first flight of SPIDER, a balloon-borne CMB telescope optimized to search for *B*-modes on degree angular scales. These data from SPIDER provide a measurement of the angular power spectra of 4.8% of the polarized sky at two frequencies: 95 and 150 GHz (SPIDER Collaboration et al. 2022). Dust emission is the dominant foreground at these at these frequencies. Since the first SPIDER instrument did not include a channel optimized for dust, the analysis of these data relies heavily on *Planck* 217 and 353 GHz maps for component separation. The published *B*-mode results from these data relied primarily on template subtraction using the XFastest power spectrum estimator (Section 2.1) alongside comparisons with alternate estimators and foreground-cleaning techniques (*e.g.*, Section 2.2).

This paper exploits the sensitivity and sky coverage of the SPIDER data to explore the properties of the Galactic emission and to quantify the impact of the methods and models employed on component separation. Section 2 reviews both component separation techniques, and in Section 3 they are applied to two distinct subsets of the SPIDER region to probe for evidence of spatial variation in the nature of the diffuse polarized dust emission. The fidelity of the MBB model is tested in a comparison of the results from the two sub-regions using two *Planck*-derived dust templates (353-

100 GHz and 217-100 GHz). Section 4 examines different choices for modeling the dust SED within the full SPIDER region: the validity of the MBB model, the constancy of MBB parameters with angular scale, and the use of power-law models for the dust angular power spectrum. Section 5 searches for LOS decorrelation by developing a custom estimator to look for evidence of variation of dust polarization angle with frequency in the SPIDER observing region. Finally, Section 6 compares the measured dust power spectrum for this sky region to templates generated by the PySM foreground modeling package.

2. COMPONENT SEPARATION TECHNIQUES

As in SPIDER Collaboration et al. (2022), our analyses in this paper rely on two main component separation techniques: foreground-template subtraction, and Spectral Matching Independent Component Analysis (SMICA). In this section, we present baseline versions of these methods. In Sections 3 and 4 we explore variations in the assumptions presented below in order to test our understanding of the polarized emission from interstellar dust.

2.1. Template Subtraction

In the baseline cosmological analysis of the SPIDER first flight data (SPIDER Collaboration et al. 2022), we remove polarized dust emission from the SPIDER 95 and 150 GHz maps by subtracting from them a scaled template for this emission derived from *Planck* data.² The SPIDER implementation of foreground-template subtraction follows the approach pioneered by Page et al. (2007) in the analysis of the *WMAP* polarization data. Within any given map pixel observed at frequency ν , the measured Stokes parameters, S_ν , are each modeled as the sum of three components: CMB, dust, and noise:

$$S_\nu = S^{\text{CMB}} + A_{\nu,\nu_0} S_{\nu_0}^{\text{dust}} + n_\nu. \quad (2)$$

The uniform (pixel-independent) scaling factor A_{ν,ν_0} connects the dust map at the observing frequency ν to that at the reference frequency $\nu_0 = 353$ GHz.

We construct our dust template by subtracting the *Planck* 100 GHz map from the 353 GHz map: $S_{\nu_0}^{\text{t}} \equiv S_{\nu_0} - S_{100}$. Since the CMB component is independent of frequency in these units, this removes the CMB signal at the cost of a modest increase in noise. To produce a cleaned CMB map, we scale this dust template by a fitting parameter α and subtract it from S_ν , giving

$$S_\nu - \alpha S_{\nu_0}^{\text{t}} = S^{\text{CMB}} + (A_{\nu,\nu_0} - \alpha [1 - A_{100,\nu_0}]) S_{\nu_0}^{\text{dust}} + n_\nu - \alpha n_{\nu_0}^{\text{t}}. \quad (3)$$

² In both the analyses presented in SPIDER Collaboration et al. (2022) and in this publication, we use release 3.01 of the *Planck* data (Planck Collaboration et al. 2020c) unless otherwise noted.

Here n_ν is the noise component at the frequency ν , and $n_{\nu_0}^1 \equiv n_{\nu_0} - n_{100}$.

Following [SPIDER Collaboration et al. \(2022\)](#), we use the XFaster algorithm ([Gambrel et al. 2021](#)) to fit for values of $\alpha = A_{\nu, \nu_0} / (1 - A_{100, \nu_0})$ and the tensor-to-scalar ratio, r , in a simultaneous fit to the SPIDER EE and BB spectra. Note that, before subtraction, the dust template is “reobserved,” *i.e.*, injected as an input sky through the full SPIDER simulation pipeline; it is thus subjected to the same scan strategy, beam smoothing, time-domain filtering, and map-making as the sky observed by SPIDER. The reobserved template, like the SPIDER data, is corrected in map space for the temperature-polarization leakage induced by the pipeline.

The template method implements a single scalar-valued factor α for each SPIDER frequency multiplying the entire map. Thus, this method assumes that the morphology of the polarized dust emission is independent of frequency (at least between 353 GHz and 100 GHz) or, equivalently, that the dust SED is constant across the relevant sky area. Note, however, that this method does *not* impose assumptions on the dust SED itself. We will revisit this assumption in our analysis below, notably in Sections 3 and 5.

2.2. SMICA

Spectral Matching Independent Component Analysis (SMICA; [Cardoso et al. 2008](#)) is a method for constructing linear combinations among a collection of maps in order to isolate desired sky components (*e.g.*, dust or CMB). In contrast to the map-space template analysis described above, SMICA operates in multipole space, acting on the spherical harmonic coefficients, $a_{\ell m}$, for each map. Given a collection of n input frequency maps,³ we construct $\mathbf{Y} = (y_1, \dots, y_n)$, where each y_i is a row vector of $a_{\ell m}$ coefficients for a single map i . We use the SMICA algorithm to construct the column vector of map weights, w , such that the linear combination $s \equiv w^T \mathbf{Y}$ is an estimate of the spherical harmonic coefficients for our desired sky component. Throughout this section, lower case letters denote vectors, and upper case bold letters denote matrices.

The weights are optimized with respect to some model of the assumed sky components. Given a column vector, a , containing the frequency scaling of a given sky component across the various maps (uniform for CMB, MBB for dust), the multipole-binned weights, w_b , for this sky component are given by

$$w_b^T = \left(a^T \tilde{\mathbf{R}}_b^{-1} a \right)^{-1} a^T \tilde{\mathbf{R}}_b^{-1}, \quad (4)$$

³ Throughout this paper, $n = 6$: for each polarization mode we use maps at all four polarized *Planck* HFI frequencies (100, 143, 217, and 353 GHz) and the two SPIDER frequencies (95 and 150 GHz).

where $\tilde{\mathbf{R}}_b$ is the binned modeled covariance matrix containing CMB, dust, and noise components. These weights minimize the variance of the reconstructed harmonic map, $\text{var}(s) = w_b^T \tilde{\mathbf{R}}_b w_b$ under the signal-preserving constraint $w_b^T a = 1$ ([Hurier et al. 2013](#)).

When reconstructing component maps, each harmonic mode $a_{\ell m}$ is scaled by the corresponding w_b for its appropriate bin. The reconstructed maps, S , are the inverse spherical harmonic transform of these weighted collections of harmonic modes.

SMICA’s power and flexibility lie in the freedom to impose (or relax) different assumptions about the components in this model, and thus about the relationships among the weights. As discussed in detail in [SPIDER Collaboration et al. \(2022\)](#), the SMICA implementation for the SPIDER B -mode analysis assumed a single dust component with a MBB SED. In this analysis we make two improvements to SMICA dust modeling: we do not impose an SED on the dust component, and we improve the power-spectrum estimation for the dust through a more accurate transfer function. Both changes are described further below.

In this analysis we do *not* assume a MBB dust SED, but instead fit for the dust a as for any other parameter of the model defining $\tilde{\mathbf{R}}_b$ (which includes the CMB, dust emission, and noise) using the same maximum-likelihood fitting procedure as in [SPIDER Collaboration et al. \(2022\)](#). We choose the arbitrary overall normalization of a such that its 353 GHz element is set to 1. Fitting for the dust a in this manner effectively trades precision for accuracy: the frequency-dependence of the reconstructed dust component will not be biased by any assumptions about the dust SED, but the uncertainty on the other fitted parameters (*e.g.*, the amplitude of the emission) will likely be larger; it could be smaller, but only if the SED we would otherwise assume were an especially poor description of the data.

In previous analyses ([SPIDER Collaboration et al. 2022](#)), the sky components of $\tilde{\mathbf{R}}_b$ are corrected for effects from filtering, beam smoothing, and mode-coupling kernels through a $J_{bb'}$ transfer matrix, as per [Leung et al. \(2022\)](#). While this approach is accurate for CMB spectra, the different angular power spectrum of dust make it inaccurate for an unbiased recovery of the full-sky dust spectrum, especially at larger scales. In this paper we modify the model to apply $J_{bb'}$ *only* to the CMB component, and instead apply a diagonal F_b to the foreground component. F_b is the ratio of the output to input power for each bin and is constructed from an ensemble of reobserved Gaussian dust realizations. These realizations follow a power-law scaling of amplitude with angular scale, with an exponent $\gamma = -2.30$, pivoting around $\ell = 80$.

Figure 1 shows the weights by which each SPIDER and *Planck* HFI frequency map contribute to the component maps computed by SMICA. For the dust component, the relative

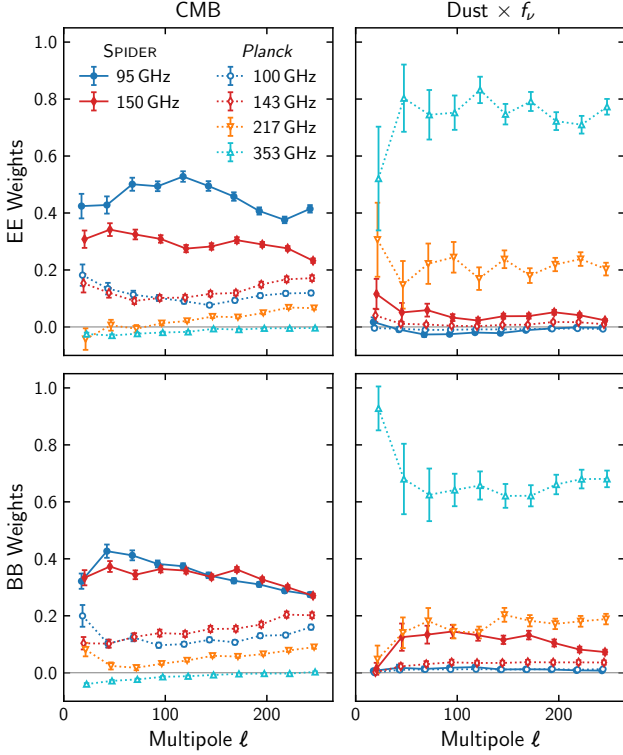


Figure 1. SMICA derived EE (top) and BB (bottom) weights to recover cleaned CMB (left) and dust (right) component Q/U maps. The SPIDER 95 and 150 GHz maps contribute predominantly toward the CMB signal, recovered (dominant positive weights) in the left panels and removed (subdominant and/or negative weights) in the right panels. The *Planck* 217 and 353 GHz maps contribute predominantly toward the dust signal, removed in the left panels and recovered in the right panels. The dust weights are scaled with the fitted dust amplitude f_ν to indicate their signal contribution.

contribution of the map at frequency ν is given by its SMICA ($a_{\ell m}$) weight multiplied by $f_\nu \equiv a_\nu^{\text{dust}}$, the ν -component of the vector a^{dust} , the dust frequency scaling vector fitted to the data by SMICA. The main contributor to both the E -mode and B -mode dust signals in Figure 1 is the 353 GHz *Planck* map, which has the highest ratio of dust signal to noise. In the B -mode dust reconstruction, all contributions are positive, as expected in the absence of CMB B -mode power.

For the CMB, the SMICA weight for a given frequency map directly represents its relative contribution, since a^{CMB} is the identity vector. The SPIDER maps provide the dominant contribution to both the E and B -modes, reflecting the higher ratios of CMB signal to noise in these maps than in any of the *Planck* HFI maps.

The Q and U maps derived by SMICA, along with their estimated uncertainties, are shown in Figures 2 and 3 for the CMB and dust components, respectively. The covariance σ_w of the weights and the noise covariance σ_γ contribute in quadrature to the total per-pixel uncertainty on the estimates

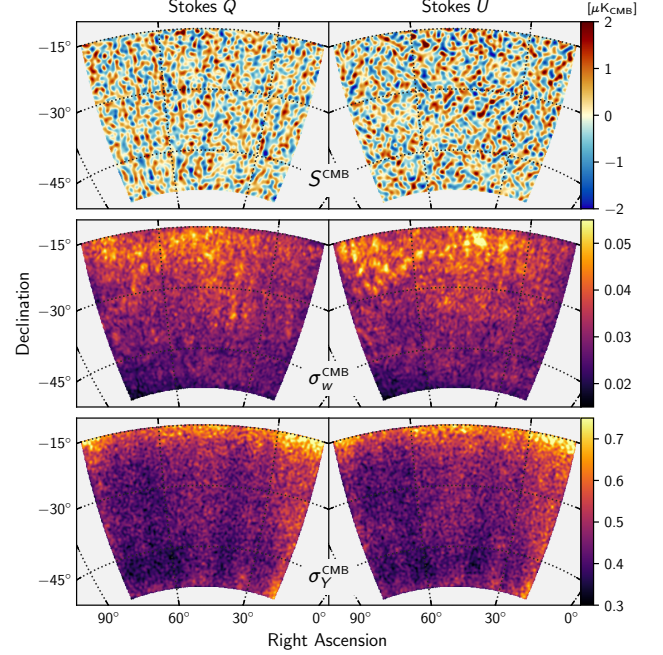


Figure 2. (top) SMICA derived component separated Stokes Q/U CMB maps computed with the CMB weights shown in the left panels of Figure 1. (middle) The contribution σ_w to the uncertainty in the CMB maps due to uncertainty in the SMICA weights. (bottom) The contribution σ_γ to the CMB map uncertainty due to the uncertainty in the input SPIDER and *Planck* data maps. All maps are in units of μK_{CMB} .

of the component maps S . The former represents the uncertainty due to signal reconstruction, while the latter (the dominant term) represents the per-pixel noise after a weighted average. Both are presented in separate panels of Figures 2 and 3.

In Figure 3, the morphology of $\sigma_\gamma^{\text{dust}}$ is similar to noise estimates for *Planck* 353 GHz, as that map dominates the weight. The uncertainty on the dust reconstruction, σ_w^{dust} , is morphologically distinct from the noise. In particular, the larger uncertainty in the upper third of the σ_w^{dust} maps does not trace the reconstructed dust signal strength or the noise. This unexpected structure could come from unidentified systematic errors in the input *Planck* or SPIDER maps, although evidence for the latter was not found in the expansive suite of null tests published in SPIDER Collaboration et al. (2022). A physical origin is also possible: frequency decorrelation, in which dust emission at a given frequency is not well correlated with that at other frequencies, would prevent an accurate reconstruction of this emission by SMICA, as the formalism here assumes that a single frequency scaling factor applies to all pixels. Given a specific frequency decorrelation model, e.g., a mixture of two dust populations, each characterized by its own spectral index, simulations could be run through SMICA in an attempt to reproduce the structure observed in the dust

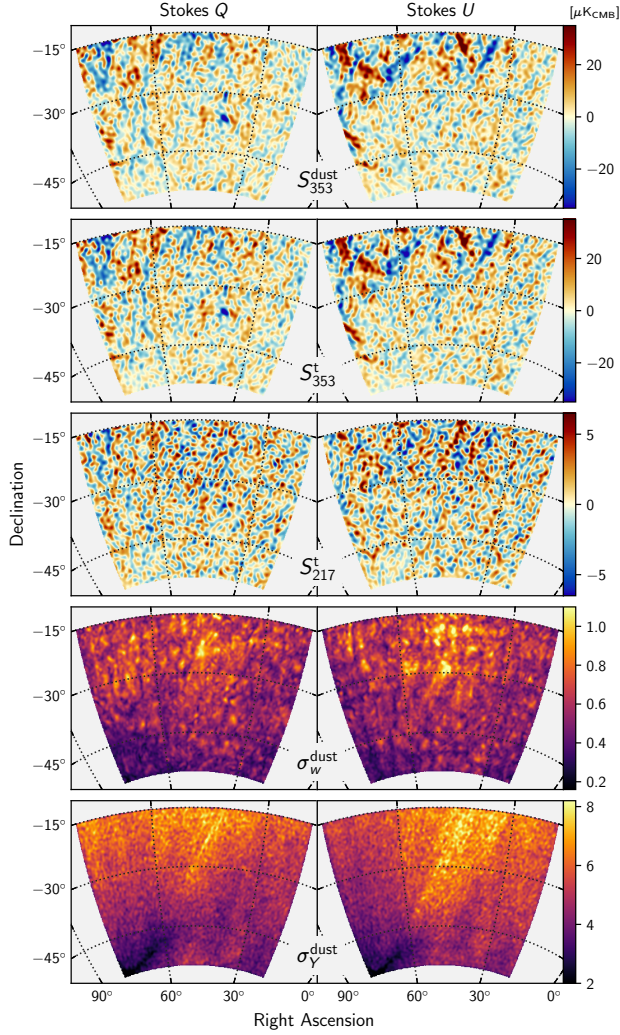


Figure 3. (row 1) SMICA derived component separated Stokes Q/U dust maps, computed with the dust weights shown in the right panels of Figure 1, and scaled to the 353 GHz reference frequency. (rows 2 and 3) The 353 GHz and 217 GHz *Planck* map templates are re-observed and band-limited to $\ell \in [8, 258]$. The SMICA dust map shows structure that is most consistent with the 353 GHz template, the predominant contribution to the component weights. (row 4) The contribution σ_w to the uncertainty in the SMICA dust maps due to uncertainty in the weights. (row 5) The contribution σ_γ to the dust map uncertainty due to the uncertainty in the input SPIDER and *Planck* data maps. Note that the morphology of σ_γ is inconsistent with that of σ_w . All maps are in units of μK_{CMB} .

uncertainty maps. Such a study is beyond the scope of our analysis.

Figure 3 also compares the SMICA dust component map S_{353}^{dust} to the *Planck* dust template maps $S_{\nu_0}^t$ constructed with $\nu_0 = 353$ GHz and $\nu_0 = 217$ GHz. The template maps have been band-limited to $\ell \in [8, 258]$, to match the scales for which SMICA weights are fit. The S_{353}^{dust} and S_{353}^t maps look very similar, which is not surprising since both are dominated

by *Planck* 353 GHz data. S_{217}^t has much lower dust amplitude than S_{353}^t , and lower signal-to-noise ratio. The visible structures in these two template maps are similar but not identical.

3. SPATIAL DEPENDENCE OF POLARIZED DUST EMISSION PROPERTIES

In our baseline cosmological analysis (SPIDER Collaboration et al. 2022), we use foreground-template subtraction (Section 2.1) to subtract the polarized emission from interstellar dust from the SPIDER maps. As reflected in the scalar nature of A_{ν, ν_0} (and therefore of α) in Equation 3, this procedure assumes that the morphology of this emission is independent of frequency. This assumption could easily be inadequate, *e.g.*, if the temperature of dust grains changes across the SPIDER region, or if two or more dust populations—even if they are well mixed—permeate it. In Section 3.2, we perform foreground-template subtraction independently in two non-overlapping, physically motivated subregions of the SPIDER field (described in Section 3.1), and assess the consistency of the α values derived in the two subregions. We discuss the physical interpretation of these results in Section 3.3.

3.1. Delineating Subregions

We define two physically motivated subregions within the SPIDER field based upon a SMICA-generated map of the total polarized dust emission power, $P^2 = Q^2 + U^2$ (Figure 4, top). This map is constructed from the Q_{353}^{dust} and U_{353}^{dust} Stokes parameter maps described in Section 2.2 and shown in Figure 3. After smoothing this map with a Gaussian of 8° FWHM, we separate the map into two complementary subregions along the $P^2 = 100 \mu\text{K}_{\text{CMB}}^2$ contour (Figure 4, bottom). We denote by P_d^+ (P_d^-) the subregion in which P^2 is greater (less) than this threshold. This procedure produces two simply-connected subregions (prior to masking point sources) that are separated by a smooth boundary, features that facilitate power spectrum estimation (Gambrel et al. 2021). After point-source masking according to the procedure described in SPIDER Collaboration et al. (2022), P_d^+ and P_d^- cover roughly equal sky fractions of 2.4% and 2.3%, respectively. We note in passing that P_d^- overlaps with the “Southern Hole,” a region of the Southern sky that has long been known to exhibit low *total* dust emission, and that has more recently been mapped with high *polarization* sensitivity (BICEP/Keck Collaboration et al. 2021; Balkenhol et al. 2023).

3.2. Template Subtraction by Subregion: Evidence for Spatial Variation

Following the procedure described in Section 2.1, we perform foreground template subtraction *independently* on each

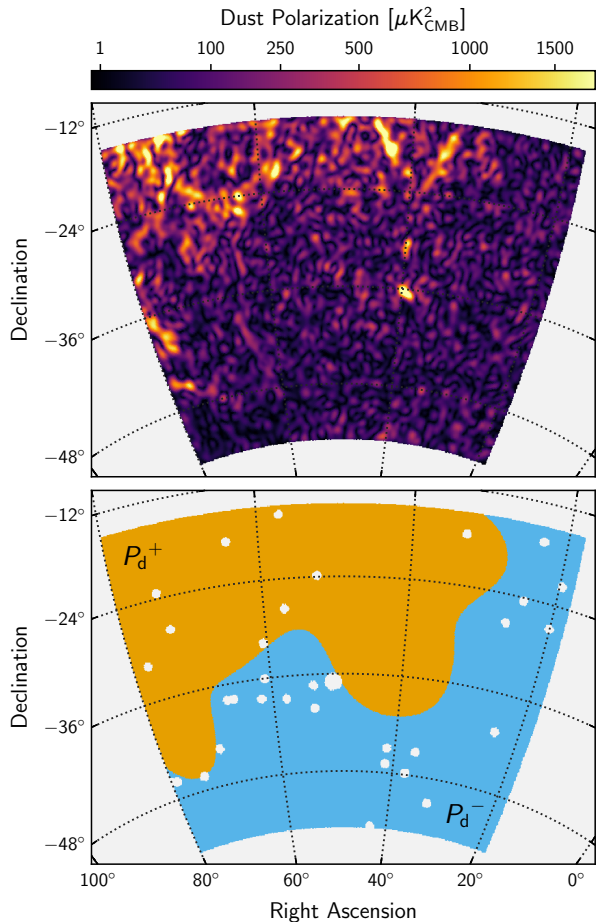


Figure 4. (top) The polarization $P^2 = Q^2 + U^2$ of the SMICA-derived dust component (first row of Figure 3). (bottom) Mask regions P_d^+ and P_d^- , containing more or less polarized dust, respectively, as inferred from the polarization map.

of the two subregions defined in Section 3.1. The left panel of Figure 5 shows, for each subregion and for the entire SPIDER field, the resulting 1-D and 2-D likelihoods for the tensor-to-scalar ratio, r , and for the foreground-template fitting parameters, α_{95} and α_{150} , where the added indices refer to the SPIDER frequencies to which we fit the *Planck* 353 GHz foreground template. Following the method in Section 4.3 of Gambrel et al. (2021), the results in this section are validated with a suite of 300 simulations with input r , α_{95} , and α_{150} fixed to the maximum likelihood values in Figure 5. Each simulated map is constructed from ensembles of CMB plus SPIDER noise, along with either the 217 or 353 GHz *Planck* dust template. Fitted templates add noise from *Planck* FFP10 realizations. To produce robust estimates of the α parameters recovered from the SPIDER data, we correct the data likelihoods for a small ($\ll 1\sigma$) bias in the XFaster estimator, as measured from this validation suite.

With the *Planck* 353 GHz template, we find the maximum-likelihood values for r and α_{95} to be consistent to better than

0.7σ and 2.0σ , respectively, between all three regions. However, the maximum-likelihood values for α_{150} differ by 3.6σ between the two subregions, with a significantly higher value of α_{150} in P_d^- than in P_d^+ . In other words, the template-correlated dust signal in the more diffuse region, P_d^- , is brighter than would be inferred by scaling the template based upon observations of the region with more polarized dust emission, P_d^+ (or of the combined region, where the fit is naturally driven by the brighter areas). We would thus expect residual dust signal after subtraction of a template that did not account for such variability.

Note that these data are *not* sufficient to establish any general causal relationship between variation in α_{150} and the intensity of the dust P map. This would require comparisons between a larger number of subregions, which is beyond the scope of this work.

We are able to reject a number of compact structures as the origin of this discrepancy. Two regions of particular interest are the Orion-Eridanus Superbubble (Finkbeiner 2003; Soler et al. 2018) and the Magellanic Stream (Mathewson et al. 1974). The former, which features prominently in H α maps, occupies about 20% of the full SPIDER region, mostly located in P_d^+ . Although the Magellanic Stream falls mostly outside the SPIDER region, some high-velocity clouds have been mapped on the outskirts of its bottom-right corner (HI4PI Collaboration et al. 2016). Even though we do not necessarily expect the dust emission from these regions to dominate the polarized emission in our maps, high levels of polarization along the edge of the Orion-Eridanus Superbubble and hints of variation in dust properties between the Galaxy and the Magellanic Clouds (Galliano et al. 2018) warrant caution. As documented in Appendix A, we find the measured spatial variation in α_{150} to be robust to masking aimed at probing the impact of these structures.

We further explore the discrepancy in α between subregions by repeating this template subtraction analysis with an alternate dust template, constructed by substituting the 217 GHz *Planck* map for the 353 GHz map. The 217 GHz data also contain substantial polarized dust emission, as evidenced by the fact that they provide the second-largest contribution to the SMICA dust reconstruction (Figure 1). The right panel of Figure 5 shows the 1-D and 2-D likelihoods for r , α_{95} , and α_{150} in this configuration. We again find r to be consistent (within 0.2σ) between the two subregions, a moderate discrepancy in α_{95} (2.7σ), and a larger discrepancy in α_{150} (3.5σ). However, while the latter discrepancy has similar significance to that found with the 353 GHz template, it is in the opposite direction: α_{150} is found to be *lower* in P_d^- than in P_d^+ .

3.3. Implications for a Modified-Blackbody Model

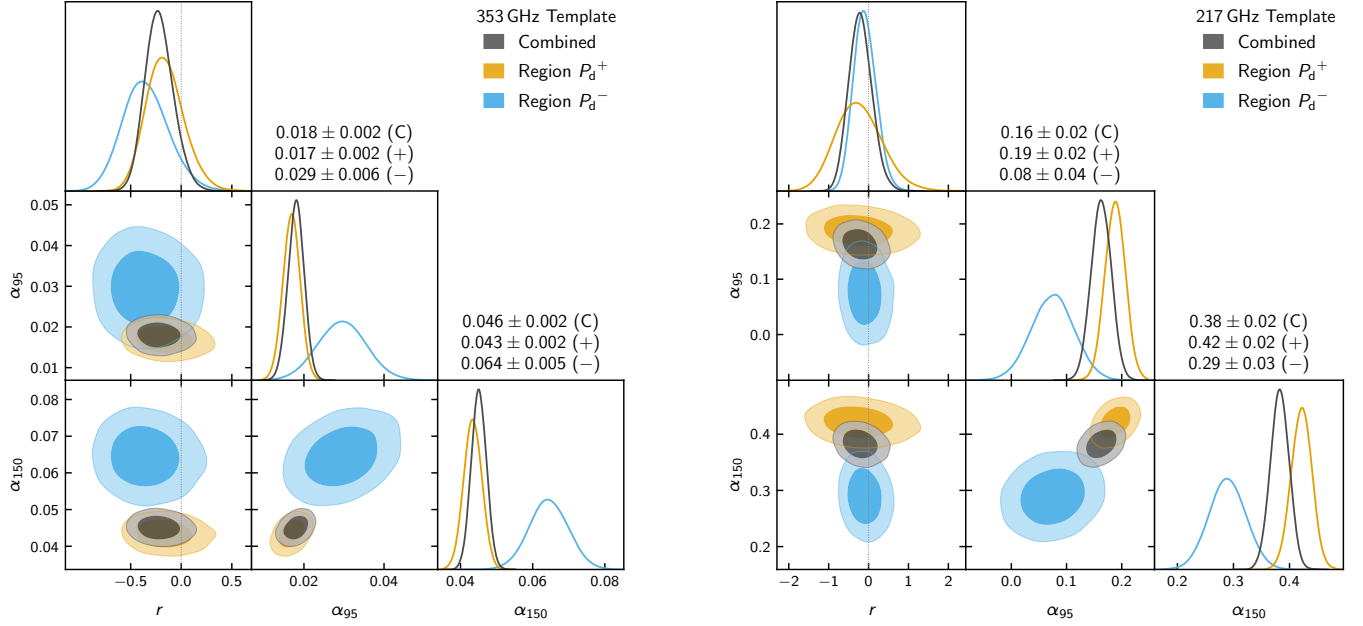


Figure 5. The XFaster likelihood contours for r , α_{95} , and α_{150} with the combined SPIDER region in gray and P_d^+ and P_d^- subregions in orange and light blue, respectively, computed independently with the 353 GHz dust template (left) and the 217 GHz dust template (right). Central values and 1σ errors for each of the three regions are indicated in the titles for the α parameters.

In the context of the simple MBB model of Equation 1, the template scaling parameter α is a function of the dust model parameters—the dust temperature, T_d , and the spectral index of polarized emission, β_d —as well as the frequencies of the maps used to build the dust template and the frequency of the map to which the template is fitted. Specifically,

$$A_{\nu, \nu_0} = \frac{(e^x - 1)^2}{x^2 e^x} \frac{x_0^2 e^{x_0}}{(e^{x_0} - 1)^2} \left(\frac{\nu_0}{\nu}\right)^2 \left(\frac{\nu^d}{\nu_0^d}\right)^{\beta_d} \frac{B(\nu^d, T_d)}{B(\nu_0^d, T_d)}, \quad (5)$$

where the superscript “d” added to the frequency of a map indicates that its effective band center is computed for a dust SED instead of the CMB SED, as discussed in Appendix B, and we have used the shorthand $x \equiv h\nu/(kT_{\text{CMB}})$.

Using this relationship, we can translate the 1-D likelihoods for α_{95} and α_{150} shown in Figure 5 into contour plots in (T_d, β_d) . The results are shown in Figure 6. These parameter constraints allow us to perform several internal comparisons within the MBB model context, which are discussed in the paragraphs below.

Comparing SPIDER frequencies—The β_d values inferred from the fitted α_{95} and α_{150} show excellent consistency ($<1\sigma$) with one another for either choice of dust template, except perhaps in P_d^+ at the very lowest dust temperatures ($T_d \lesssim 7\text{K}$). In other words, if we confine ourselves to a single *Planck*-derived dust template, the SPIDER data provide no significant evidence of deviation from an MBB SED in either subregion.

Comparing subregions—The values of α_{150} obtained using the $\nu_0 = 353\text{GHz}$ dust template translate into *lower* values of β_d in P_d^- compared to P_d^+ for any value of T_d . Specifically, if we fix $T_d = 19.6\text{K}$ (Planck Collaboration et al. 2020b) throughout, we find $\beta_d = 1.52 \pm 0.06$ in P_d^+ and 1.09 ± 0.09 in P_d^- . Importantly, the value of β_d inferred independently from α_{95} is consistent with that of α_{150} , with comparable significance. Taken at face value, this 3.9σ inconsistency in β_d would indicate a spatial variation in dust composition between the P_d^+ and P_d^- subregions.

If we instead fix the dust spectral index to be $\beta_d = 1.53$ (Planck Collaboration et al. 2020b) in both subregions, we find a large difference in implied dust temperatures: $T_d = 19.1_{-2.5}^{+3.7}\text{K}$ in P_d^+ , $T_d = 9.2_{-0.8}^{+1.1}\text{K}$ in P_d^- . Although we certainly expect *some* lack of uniformity in dust temperature—stemming from spatial variation in the dust’s radiative environment—such a large variation in the temperature of the diffuse interstellar medium at high Galactic latitude may be unphysical given our current understanding of dust physics (Li & Draine 2001; Draine & Li 2007).

A similar discrepancy between subregions (though of *opposite sign*) is visible with the 217 GHz dust template, as shown in the middle panel of Figure 6. Fixing $T_d = 19.6\text{K}$ with the α_{150} constraint results in $\beta_d = 1.37 \pm 0.08$ in P_d^+ and $2.1_{-0.2}^{+0.3}$ in P_d^- , a 3.2σ discrepancy. Alternatively, fixing $\beta_d = 1.53$ gives $T_d = 12_{-2}^{+3}\text{K}$ for P_d^+ , but no value of T_d accommodates $\beta_d = 1.53$ within P_d^- .

Comparing dust templates within P_d^- —The values of β_d derived from α_{150} within the P_d^- subregion using the $\nu_0 = 217\text{GHz}$

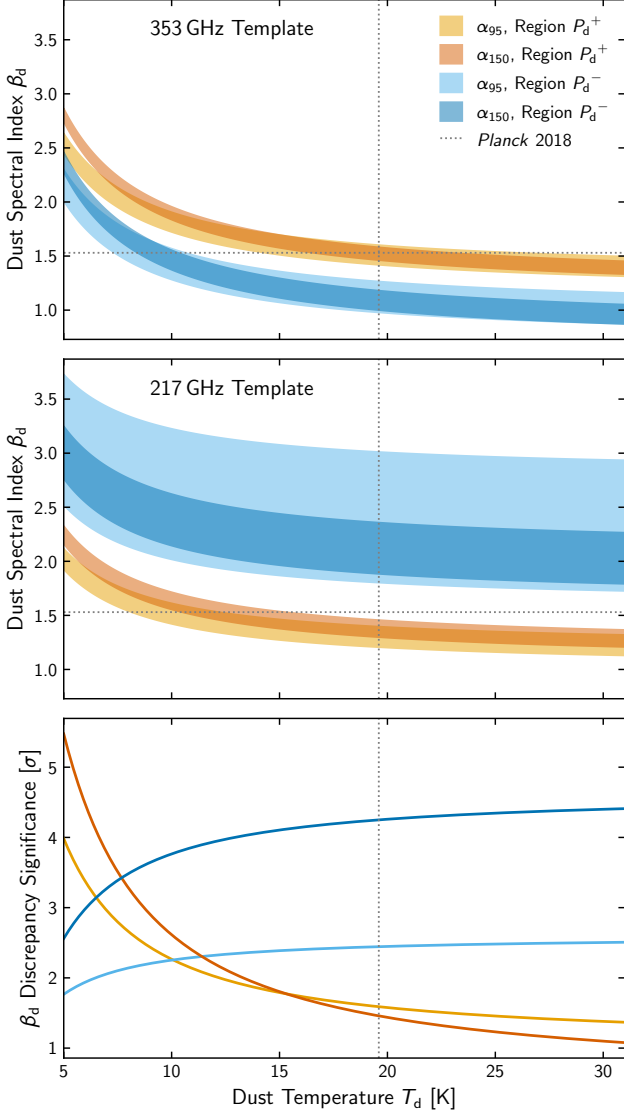


Figure 6. 1σ contours of possible T_d and β_d for the α values found with the XFastest framework and presented in Figure 5. (*top*) Using the 353 GHz dust template, the P_d^+ region is identified with a higher β_d or a higher T_d , while the P_d^- region is identified with a lower β_d or T_d . (*middle*) With the 217 GHz template, the P_d^+ region is instead identified with a lower β_d or T_d than the P_d^- region. (*bottom*) Mutual significance of the discrepancy in β_d between the two templates, as a function of assumed T_d . The β_d values found in the P_d^- region are discrepant at $> 3\sigma$, while the significance of the discrepancy is $< 2\sigma$ in the P_d^+ region. The *Planck* 2018 all-sky best fit parameters ($\beta_d = 1.53$, $T_d = 19.6$ K) are also shown for reference (*dotted lines*).

dust template are *inconsistent* with those derived using the $\nu_0 = 353$ GHz template. The bottom panel of Figure 6 shows the significance of this discrepancy as a function of dust temperature: it exceeds 3σ (4σ) for any $T_d \gtrsim 5$ K ($T_d \gtrsim 15$ K). Under the assumption that the morphology of the polarized emission from interstellar dust is identical in both templates, this result corresponds to a statistically significant break in

β_d for any physical T_d , with the index having a lower value at the higher frequency.

Furthermore, we find that the value of α_{150} *increases* from P_d^+ to P_d^- with the $\nu_0 = 353$ GHz template, but *decreases* from P_d^+ to P_d^- with the $\nu_0 = 217$ GHz template. This observation is difficult to interpret under the assumption that the morphology of the polarized emission from interstellar dust is identical in both templates. This can be reconciled by assuming the existence of more than one dust population (which may be inferred from the spatial variation in β_d detected with the $\nu_0 = 353$ GHz template) *combined with* a break in β_d between 217 and 353 GHz.

Discussion—The physical interpretation in this section of the results derived in Section 3.2 points to a more complex picture of the polarized emission from interstellar dust in the SPIDER region than that provided by a single-component MBB model.

Taking the observations above together, we conclude: *i*) Unless T_d exhibits large variations at high Galactic latitudes, the spatial variation in α between P_d^+ and P_d^- may be evidence of *multiple dust populations* (*i.e.*, differing compositions, and thus emissivities); *ii*) Unless the $\nu_0 = 217$ GHz dust template is morphologically inconsistent with the $\nu_0 = 353$ GHz template, the inconsistency between the value of α derived in P_d^- with one template and that found in the same subregion with the other template would indicate a *break in the value of β_d between 217 and 353 GHz*; *iii*) The break in β_d may itself be *composition dependent* in order to simultaneously explain the increase in α between P_d^+ and P_d^- observed with the $\nu_0 = 353$ GHz template and its decrease obtained with the $\nu_0 = 217$ GHz template. If this rather complex picture holds as more data (such as the SPIDER 280 GHz maps) become available, it may provide new insights into the properties of the interstellar medium, and associated modeling uncertainties would need to be taken into account in upcoming searches for cosmological *B*-modes.

4. TESTING STANDARD DUST MODELING

The SMICA framework offers a high degree of flexibility in modeling the characteristics of dust. The SMICA pipeline implemented for the analysis in *SPIDER Collaboration et al. (2022)* incorporates a MBB model for the dust foreground component with the following characteristics:

- A single β_d parameter that is common across all multipoles and polarizations,
- A dust amplitude A_d that is free to vary across multipoles and polarizations,
- A δ -function prior of $T_d = 19.6$ K to fix the dust temperature at the *Planck* all-sky value, and
- A Gaussian prior on β_d centered at the *Planck* all-sky value $\beta_d = 1.53$, with a generous width of $\sigma_{\beta_d} = 1.5$.

Table 1. The best-fit dust amplitude A_d for each of the input frequency maps relative to that of the *Planck* 353 GHz map. The values tabulated here are also plotted in Figure 7. Best-fit values are computed as the median of the posterior distribution, with 1σ errors determined from the 68% interval on either side of the median.

Instrument	Band	Dust Amplitude	
		EE	BB
SPIDER	95 GHz	0.019 ± 0.005	$0.016 \pm_{-0.004}^{+0.005}$
	150 GHz	$0.047 \pm_{-0.004}^{+0.005}$	0.047 ± 0.003
<i>Planck</i>	100 GHz	$0.018 \pm_{-0.006}^{+0.005}$	0.028 ± 0.007
	143 GHz	0.043 ± 0.008	0.039 ± 0.010
	217 GHz	0.139 ± 0.013	0.123 ± 0.014

In this section, we quantify how these foreground modeling choices impact the best-fit CMB and foreground parameters recovered with the combined SPIDER and *Planck* data. Throughout this section, we leave the dust temperature fixed, due to a lack of sufficient constraining power and frequency coverage to simultaneously estimate both β_d and T_d , while varying the constraints on A_d and/or β_d . Here, unlike the discussion in Section 3.3, we apply the analysis to the full SPIDER region. The results in this section are therefore driven by the higher signal-to-noise component, corresponding approximately to the P_d^+ contours of Figure 6.

4.1. SED Modeling of Polarized Dust Emission

We begin by testing the SED model of dust emission by fitting an independent amplitude A_d at each frequency, operating under the assumption that this amplitude remains consistent across multipoles. As discussed in SPIDER Collaboration et al. (2022), dust and noise exhibit similar scaling behaviors with frequency, making it challenging for an ICA-based algorithm to distinguish between the two components. By relaxing the prior constraint on β_d and fitting for the dust amplitudes directly, we are able to circumvent this noise/dust scaling degeneracy. The resulting amplitudes can then be fit to a MBB model to recover the best-fit β_d value.

The dust amplitudes recovered with this algorithm are listed in Table 1 for each of the SPIDER and *Planck* frequency bands, and the resulting MBB model fit is illustrated in Figure 7. Fitting a spectral index to each set of six frequency maps results in a best-fit value of β_d of 1.45 ± 0.05 (1.47 ± 0.06) for the *EE* (*BB*) components, with χ^2 values of 0.7 (3.0), respectively.⁴ With approximately four degrees of freedom, these χ^2 values indicate that a single-component MBB model is an adequate description of the SPIDER +

⁴ For comparison, we note that the template fit in the combined region from Section 3.3 corresponds to a value $\beta_d = 1.50 \pm 0.05$ for the combined *EE* & *BB* spectra.

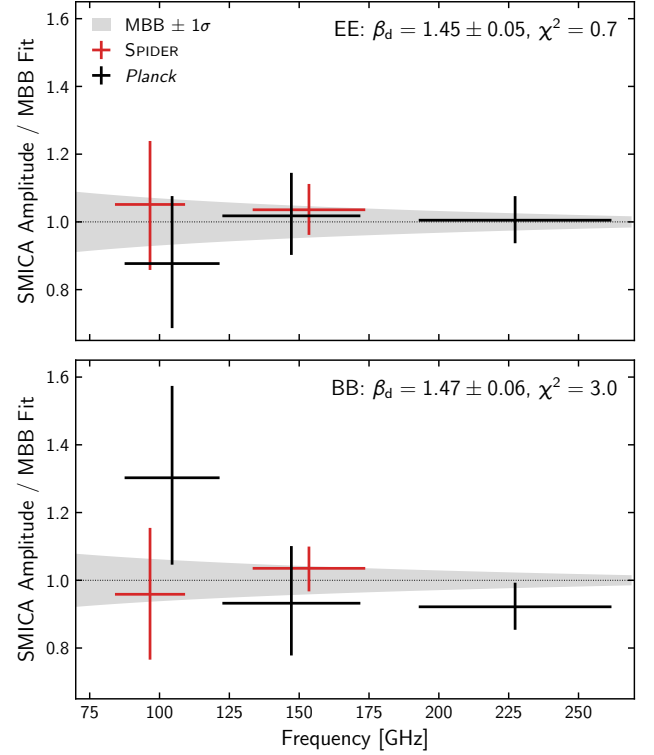


Figure 7. Testing the fidelity of the MBB dust model in the SPIDER high-latitude region for *E*- (top) and *B*- (bottom) modes. All data are plotted relative to the best-fit MBB model for that polarization component (gray band indicates the 1σ fit envelope), and account for the detector bandpass at each frequency. The horizontal error bars indicate the effective detector bandwidth over which the amplitudes are computed. The SMICA best-fit dust amplitudes (+) are consistent with the best-fit MBB model. The SPIDER data (red) have smaller error bars on A_d , and therefore more constraining power, than the *Planck* data (black) in nearby bands.

Planck dataset, thus justifying the use of the MBB model for constraining foreground power in the CMB *B*-mode analysis. Additionally, Figure 7 illustrates the improved constraining power of the SPIDER data at 95 and 150 GHz in this region of the sky relative to that of the nearby *Planck* bands at 100 and 143 GHz.

4.2. Angular Scale Dependence of Dust Spectral Index

Next we test the assumption of a scale-independent SED by fitting the MBB model independently for each polarization as a function of ℓ . The results of this fit for β_d are shown in Figure 8. The best-fit spectral index values agree to within $\sim 0.5\sigma$ between the *E* and *B* polarization components across all angular scales, providing no evidence for including a polarization-dependence in the model. Comparing the best-fit β_d values averaged over larger ($\ell < 140$) and smaller ($\ell > 140$) angular scales shows agreement to within 2σ .

When analyzed over the full SPIDER region, the data do not reveal any strong evidence of variations in spectral index

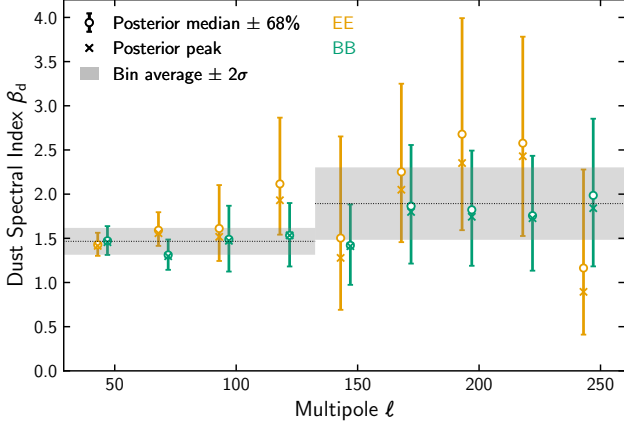


Figure 8. An analysis of the variation of the dust spectral index over angular scale using the SMICA pipeline. Each point covers a binned multipole range of $\Delta\ell = 25$, with E and B points offset in ℓ for clarity. The distributions of the best fit β_d in each bin are not Gaussian; the median (\circ) and peak (\times) of each posterior are indicated. The error bars correspond to 68% intervals on either side of the median, equivalent to 1σ for a non-Gaussian distribution. The best-fit β_d values agree to within a mutual 2σ between the larger and smaller angular scales. The E and B β_d values are statistically consistent with each other at all scales.

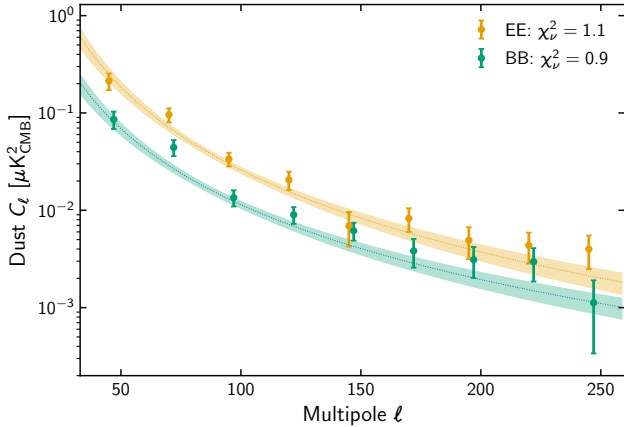


Figure 9. A power-law model fit to the SMICA-derived dust amplitudes as a function of angular scale. The best-fit model, shown as a band indicating the 1σ error on the fit, is binned identically to the SMICA-derived dust bandpowers in order to compute the χ^2 of the fit. The reported χ^2_ν values are computed using the full covariance of both the power-law model and the SMICA bandpowers, and assume seven degrees of freedom. The best-fit model parameters are shown in Figure 10.

with polarization mode or angular scale, further justifying the adoption of the simple MBB dust model.

4.3. Angular Scale Dependence of Dust Amplitude

Dust emission is often (e.g., Planck Collaboration et al. (2020b); BICEP/Keck Collaboration et al. (2021)) modeled

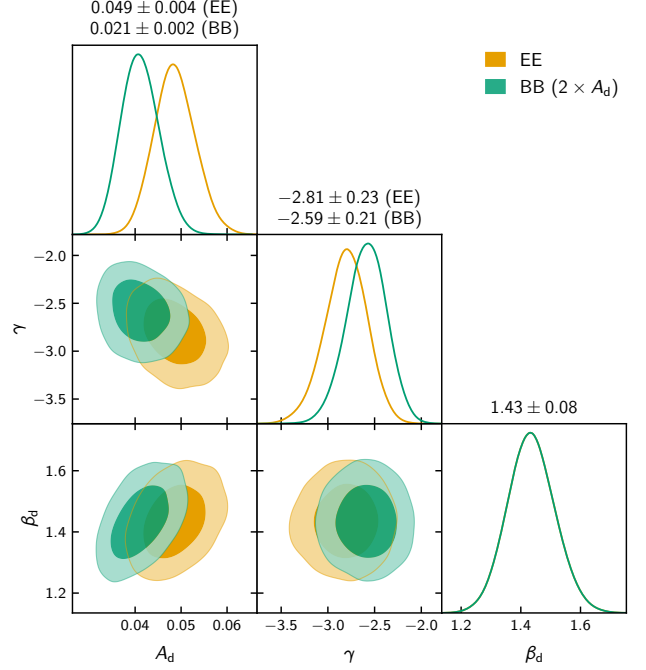


Figure 10. The covariance of the fitted dust parameters for the model shown in Figure 9. Central values with 1σ errors are indicated in the titles for each of the three parameters. The best-fit A_d and σ_{A_d} for the BB component is scaled by a factor of 2 for better visual comparison to its EE counterpart, with its true central value indicated in the column title.

as a power law in C_ℓ :

$$C_\ell = A_d(\nu) \left(\frac{\ell}{80} \right)^\gamma. \quad (6)$$

We can fit this model to the SMICA-derived amplitudes as a function of ℓ -bin independently for the E and B polarization components. We assume a single-component MBB scaling of the amplitude with frequency, common to both polarizations. The results of this fit are shown in Figures 9 and 10, with reduced $\chi^2_\nu = 1.1(0.9)$ for the E (B) polarization components, assuming $\nu = 7$. This analysis finds a dust spectrum that falls steeply, $\gamma^{EE} = -2.81 \pm 0.23$, with no significant difference in best-fit values between the two polarizations. We note that *Planck* has reported values of -2.42 and -2.54 ± 0.02 in the largest area of sky for EE and BB , respectively. In the most restrictive mask, *Planck* finds more shallow indices of -2.28 ± 0.08 and -2.16 ± 0.11 for EE and BB (Planck Collaboration et al. 2020b).

The SPIDER dataset also provides an additional observational constraint on the asymmetry in dust power between EE and BB polarization modes, visible in Figure 10. This analysis finds an EE/BB dust power ratio of 2.1 ± 0.3 at large scales ($\ell < 140$). This result aligns with prior findings from *Planck* (Planck Collaboration et al. 2016a). The origin of this dust power asymmetry is not conclusively understood.

Some studies investigate the role of magnetohydrodynamic (MHD) turbulence in the interstellar medium (ISM) (Caldwell et al. 2017; Kandel et al. 2017), while others suggest that this power asymmetry can be a probe of the dust filament aspect ratio (Huffenberger et al. 2020) and magnetic field alignment (Clark et al. 2021).

4.4. Impact on Cosmological B-mode Measurements

At the level of sensitivity of contemporary observational programs, the contribution of modeling uncertainty to limits on the cosmological CMB B-mode signal is non negligible even in those regions of the sky with low levels of Galactic emission. In this section we attempt to quantify the impact of these complexities on the uncertainty in the tensor-to-scalar ratio, σ_r , within the SPIDER region.

Following the analysis in SPIDER Collaboration et al. (2022), for each dust model we can compute the σ_r derived from an ensemble of sky and noise simulations constructed to match the model under consideration. In the configuration where there is no SED modeling and SMICA fits a dust amplitude per frequency, we find $\sigma_r = 0.130$. If instead a spectral index β_d is fit per multipole, allowing for dust behavior to change with scale, we find $\sigma_r = 0.128$. Constraining the spectral index to a single value over all scales, as in SPIDER Collaboration et al. (2022), we find $\sigma_r = 0.116$. Finally, the assumption that dust follows a power-law in multipole space *does not* improve σ_r further. We find instead that this assumption re-distributes the uncertainties: the uncertainty near the pivot scale ($\ell \sim 80$) is reduced, while that at larger scales increases. Thus, we find that the complexities in foreground modeling described in this section can contribute at the level of $\sigma_r \sim 0.012$, corresponding to a $\sim 10\%$ impact on σ_r in the case of SPIDER.

4.5. Discussion

When applied to the full area of sky observed by the SPIDER experiment, the variations of the nominal SMICA algorithm described above, each employing different assumptions about foreground modeling, all point to a consistent description of polarized Galactic dust emission. These data are consistent with dust characterized by a single-component, modified black-body model across the SPIDER and *Planck* frequencies and for both polarization parity modes. The dependence on angular scale is consistent with an approximate power-law dependence on multipole, ℓ . The combined SPIDER and *Planck* data over this restricted region prefer a dust emissivity spectral index $\beta_d = 1.45 \pm 0.07$, somewhat lower than the all-sky *Planck* 2018 value (Planck Collaboration et al. 2020b) of $\beta_d = 1.53 \pm 0.02$ with $T_d = 19.6K$. The foreground complexities considered in this section are found to contribute to the uncertainty on the tensor-to-scalar ratio at the level of $\sigma_r \sim 0.012$.

5. LINE-OF-SIGHT DECORRELATION OF DUST

In addition to the search for spatial variation in Section 3, we use SPIDER data to perform a search for variation in the polarization angle of dust emission with frequency. Such a rotation with frequency may indicate the presence of multiple dust clouds along a line of sight with different SEDs and magnetic alignments. For example, (Pelgrims et al. 2021) used HI line emission maps to identify regions of the sky likely to contain magnetically-misaligned clouds; they compute the difference in polarized dust angle for these different populations to demonstrate that LOS frequency decorrelation is detectable within the *Planck* dataset, largely in the Northern Galactic cap. An analysis by the BICEP team (BICEP/Keck Collaboration et al. 2023) showed no evidence of dust decorrelation within their observation region.

We perform this search by constructing a set of dust templates as in Section 2.1, each derived from a single SPIDER or *Planck* map. In this case, we opted to subtract CMB signal using the SMICA-derived CMB template rather than the *Planck* 100 GHz map, due to its lower overall noise level. From each template, we compute a map of polarized dust angle using the unbiased estimator (Plaszczynski et al. 2014)

$$\psi = \frac{1}{2} \arctan(U, Q). \quad (7)$$

We construct a likelihood estimator to evaluate the consistency of the measured dust angle ψ at different frequencies.

In order to construct our likelihood, we approximate the uncertainty on ψ as Gaussian. We estimate this uncertainty with standard error propagation:

$$\sigma_\psi^2 = \frac{1}{4} \frac{Q^2 \sigma_U^2 + U^2 \sigma_Q^2}{(Q^2 + U^2)^2} + \frac{Q^2 U^2}{2(Q^2 + U^2)^4} \left[\sigma_Q^4 + \sigma_U^4 + \frac{1}{2} \frac{(Q^2 - U^2)^2}{Q^2 U^2} \sigma_Q^2 \sigma_U^2 \right] \quad (8)$$

where the two grouped terms represent the first- and second-order errors respectively. We expect these uncertainties to be underestimated when the signal-to-noise is low ($\sigma_U^2 + \sigma_Q^2 > U^2 + Q^2$). However, the Gaussian approximation breaks down as higher-order terms become more significant. To address this, we apply a mask to reject map pixels for which the second-order errors on polarized dust angle exceed the first. This criterion rejects 20-30% of the sky area covered by the SPIDER instrument. This thresholding serves two main purposes: (1) to exclude pixels whose uncertainties are challenging to model accurately, and (2) to remove pixels with especially large uncertainties, for which the width of the distribution would wrap around the range of the arctangent function, yielding non-Gaussian behavior. While the statistical properties of ψ are complex and cannot be strictly Gaussian, the Gaussian distribution serves as a reasonable approximation after this thresholding.

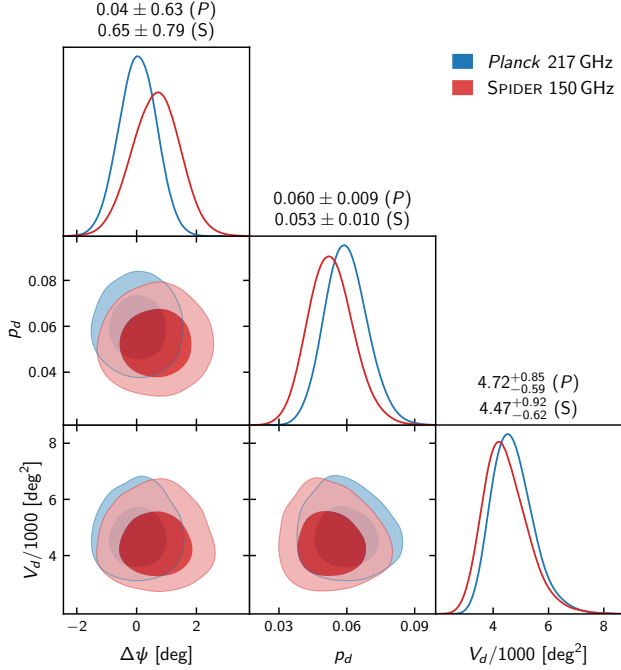


Figure 11. Best-fit model parameters for the dust angle decorrelation likelihood defined in Equation 9: global dust angle offset $\Delta\psi$ in degrees, population fraction p_d of pixels with measurable angle differences, and additional variance V_d in square degrees introduced by these outlier pixels. We find that $\Delta\psi$ is statistically consistent with zero, indicating that the dust angle appears globally consistent between the *Planck* 353 GHz frequency map and lower frequencies *Planck* 217 GHz (blue) and SPIDER 150 GHz (red). The likelihoods are marginalized over $\{q_i\}$, and central values with 1σ errors are indicated in the titles.

From a given pair of dust maps X and Y we calculate a pair of dust angles (ψ_i^X, ψ_i^Y) for each map pixel i . To this we fit a Gaussian mixture model (Hogg et al. 2010) in which each pixel can belong to one of two populations: a base population, for which the dust angle is *consistent* between our pair of maps up to some constant angular offset $\Delta\psi$; and a second population of outlier pixels, for which the polarization angle is *inconsistent* between the two frequencies. The first population probes a possible systematic offset in polarization angle between maps at different frequencies; this is expected to be consistent with zero, and unlikely to arise from dust decorrelation given the relatively large sky area covered by SPIDER. The second population is our probe of decorrelated dust, in the form of isolated, dense cloud structures with arbitrary polarization angles relative to our line of sight.

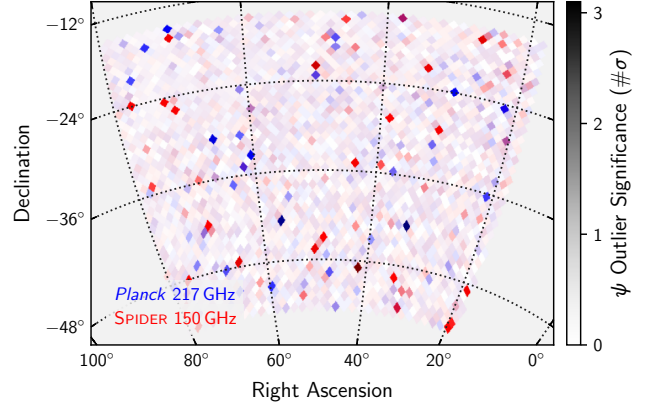


Figure 12. The significance in σ of the probability p_i that the measured dust angle in each map pixel i is inconsistent between the *Planck* 353 GHz map and either the *Planck* 217 GHz map (blue) or the SPIDER 150 GHz map (red). The significance is encoded such that bright purple pixels are likely in the outlier population in both frequency pair analyses. The lack of both astrophysical structure and overlap between the two populations argues against local decorrelation in the SPIDER observing region.

Our likelihood takes the form

$$\mathcal{L}(\{q_i\}, \Delta\psi, p_d, V_d) = \prod_i \left[\frac{1}{\sqrt{2\pi}\Sigma_i} \exp\left(-\frac{\Delta_i^2}{2\Sigma_i}\right) \right]^{1-q_i} \times \left[\frac{1}{\sqrt{2\pi}(\Sigma_i + V_d)} \exp\left(-\frac{(\psi_i^X)^2 + (\psi_i^Y)^2}{2(\Sigma_i + V_d)}\right) \right]^{q_i}, \quad (9)$$

where

$$\Delta_i = \min_{\delta_\pi} \left\{ \frac{1}{\sqrt{2}} \left((\psi_i^Y + \delta_\pi) - (\psi_i^X + \Delta\psi) \right) \right\} \quad (10)$$

$$\Sigma_i = \frac{1}{2} (\sigma_X^2 + \sigma_Y^2) \quad (11)$$

$$q_i \sim \text{BetaBinomial}(\alpha = p_d, \beta = 1 - p_d) \quad (12)$$

The boolean q_i assigns each pixel i to one of the two populations. The generative model of the base population ($q_i = 0$) is taken to be a two-dimensional Gaussian, with an orthogonal distance Δ_i between the two map angles for each pixel (Equation 10) and variance Σ_i (the projected variance of the uncertainty of the pixel onto a line of slope of unity). Note that, because the domain of angles lies in the range $[-\pi/2, \pi/2]$, differences in ψ by any multiple of π are inconsequential. We account for this by minimizing over a nuisance parameter $\delta_\pi \in \{-\pi, 0, \pi\}$ in Equation 10.

The second population represents outlier, or rejected, pixels, which show local differences in angle between the maps. We do not *a priori* have an expectation for the statistics of this population. We choose to model it as a two-dimensional

Gaussian with zero mean and an additional variance V_d (in excess of Σ_i).

Finally, we treat the pixel assignments q_i probabilistically, such that each pixel has a probability p_i of being assigned to the base population. The probability p_i is itself drawn from a beta distribution with $\alpha = p_d, \beta = 1 - p_d$, such that the expectation value $E(p_i) = p_d$. In this way, p_d can be thought of as a global parameter for the fraction of outlier pixels in the total population. All together, our model has $N_{\text{pix}} + 3$ variables: N_{pix} population assignments q_i , a systematic offset parameter $\Delta\psi$, and two parameters describing the variance (V_d) and population fraction (p_d) of the outliers.

We conduct two iterations of this analysis using pairs of maps with the highest signal-to-noise ratios for dust: one comparing the *Planck* 353 GHz and SPIDER 150 GHz maps, the other comparing *Planck* 353 GHz to *Planck* 217 GHz. Figure 11 shows the resulting uncertainties and covariances between the fit parameters ($\Delta\psi, p_d, V_d$). Both comparisons find angular offsets $\Delta\psi$ consistent with zero to within 1σ , with p -values of 0.21 (0.47) for $\Delta\psi_{150}$ ($\Delta\psi_{217}$). This suggests that the mean polarized dust angle at 353 GHz is consistent with those at lower frequencies.

Only about 5% of the pixels included in our analysis region are rejected and assigned to the outlier population. These pixels display discrepancies in dust angle between 353 GHz and the corresponding lower frequency. While these outliers could signify spatially-dependent decorrelation, a map of the locations of these pixels (Figure 12) reveals two key observations: (1) the regions lack the connectivity we might expect from a real astrophysical population, and (2) the outliers identified by the two analyses share little overlap. Indeed, only about 0.2% of pixels are identified as deviant in both analyses. This argues against interpreting these pixels as a detection of LOS decorrelation.

We can further perform a hypothesis test to estimate the probability of this analysis yielding 5% decorrelated pixels under the null hypothesis that there is no decorrelated dust at any frequency for the entire observed region. We construct a dust map from 353-100 GHz difference maps, then scale this to both 150 GHz and 217 GHz using a standard modified black-body dust model. To this we add realistic noise by drawing from an ensemble of simulations, specifically SPIDER noise simulations at 150 GHz and *Planck* FFP10 realizations at 217 GHz and 353 GHz. From these simulated dust + noise maps, we compute the dust angles and perform an identical analysis. Comparing our measurement of the fraction of outlier pixels, p_d , to this ensemble of simulations, we obtain p -values of 0.18 and 0.10, respectively, for the 150 GHz and 217 GHz analysis. We thus conclude that the inferred fraction of decorrelated pixels can be readily attributed to noisy measurements of Stokes Q and U . Consequently, our analysis finds no evidence for LOS decorrelation in the SP-

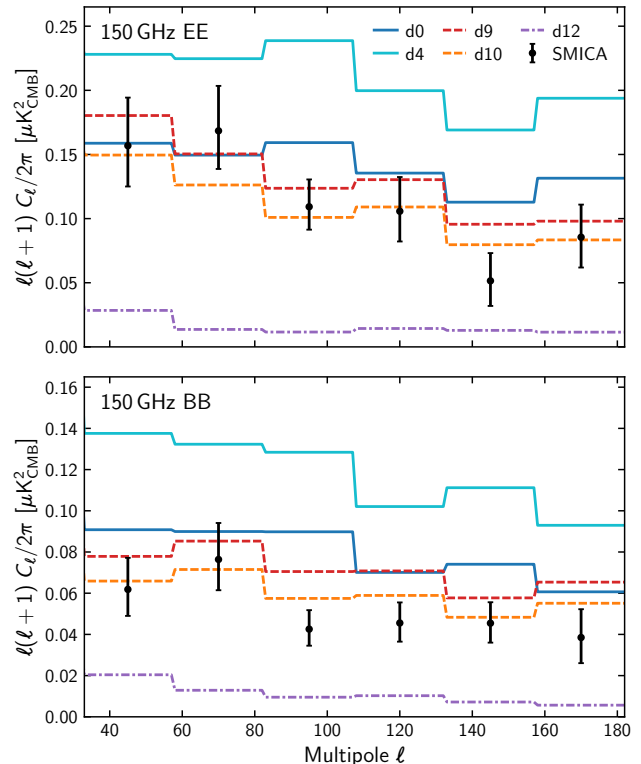


Figure 13. Comparison of the *EE* (top) and *BB* (bottom) spectra from several PySM3 dust models (colored lines) to SMICA-derived dust bandpowers at 150 GHz (black points) in the SPIDER region. Models based on the same underlying inputs and approach to SED modeling are shown with the same line style.

DER observing region. The dust angles at 353 GHz largely agree with those at the lower frequencies, and those pixels that show oversized deviations are plausibly caused by noise.

6. COMPARISON TO PYSM DUST MODELS

The SMICA dust maps derived from the combination of SPIDER and *Planck* data (shown in Figure 3) can also be used to test full-sky dust models. The Python Sky Model, commonly known as PySM, is a Python package designed for generating full-sky simulations of Galactic microwave foregrounds (Thorne et al. 2017). It is often used by the CMB community to test component separation methods and perform sensitivity forecasts. The current release, PySM3, contains thirteen distinct dust models that vary the assumptions and data processing of the underlying *Planck* data, allowing the user to generate full-sky dust emission maps at any frequency bandpass of interest.

To test the agreement between each of these models and our SMICA dust polarization maps, we first use PySM to generate maps in the SPIDER observing region using the measured 150 GHz frequency bandpass. We then compute binned *EE* and *BB* spectra for each PySM model using POLSPICE (Chon et al. 2004) and compare these to analo-

gous spectra generated from the SPIDER-*Planck* SMICA dust maps described in Section 2.2.

Figure 13 shows these spectra for a representative subset of dust models, which were chosen to span the range of predicted dust amplitudes in the SPIDER observing region and highlight several that have been used in recent experiment forecasts (e.g. The Simons Observatory Collaboration et al. (2019); Abazajian et al. (2016)). Briefly, each of these are described as follows:

- **d0**: A single-component MBB with fixed ($\beta_d = 1.54$, $T_d = 20\text{ K}$) using the *Planck* 2015 353 GHz polarization map (Adam et al. 2016) as a template.
- **d4**: A generalization of the MBB model with spatially varying temperature and spectral index based on the *Planck* 2015 results, scaled using the two-component model from Finkbeiner et al. (1999).
- **d9**: A single-component MBB model with fixed ($\beta_d = 1.48$, $T_d = 19.6\text{ K}$) based on the *Planck* 2018 results (Planck Collaboration et al. 2020b), which uses GNILC component-separated maps as a template (Planck Collaboration et al. 2020d) with additional small-scale fluctuations.
- **d10**: A variant of **d9** that also includes small-scale fluctuations in β_d and T_d .
- **d12**: A 3-D model of polarized dust emission with six layers as further described in Martínez-Solaache et al. (2018).

More information about each of these models can be found in the PySM documentation.⁵ The remaining PySM3 models are compared in Appendix C and Figure 15.

From these figures we can make some qualitative observations about how these models behave in this region of the sky. For instance, the similarity in predicted power between models **d0** and **d9** suggests that differences in the model parameters and templates between the *Planck* 2015 and 2018 releases do not greatly affect the degree-scale dust predictions in this region of sky. The scale of variation between **d10** and **d11** reflects the impact of stochastic modeling of the small scale features. On the other hand, despite their common underlying *Planck* data, several of these models predict substantially different dust levels from the others in this region. In particular, **d4** predicts significantly more degree-scale polarized dust emission than the other models while **d12** predicts significantly less, though a detailed exploration of the origin of these differences is beyond the scope of this work.

Comparing the PySM spectra with those from our SMICA analysis is complicated by the fact that both SMICA and the

various PySM models draw heavily upon the same underlying *Planck* maps and noise ensembles. In our own SMICA analysis, for example, the *Planck* 353 GHz map dominates the relative weights used to construct the dust component and thus drives the morphology of the dust map and the *shapes* of the dust power spectra. The *amplitudes* of those power spectra at 150 GHz, however, are driven primarily by the SPIDER data. Since different PySM models employ the *Planck* maps in different ways and combinations, we expect complex covariances among all of these spectra that are difficult to quantify reliably. We can nonetheless qualitatively observe closer correspondence of our on-sky results with some models (e.g., **d0**, **d9**, **d10**) than others (e.g., **d4**, **d12**).

7. CONCLUSION

This paper addresses the impact of choices made in component separation for the SPIDER cosmological *B*-mode analysis, and explores the complexity of the polarized dust emission in the SPIDER region. A quantitative comparison of a template-based and harmonic-independent-component analysis shows that, at the level of the statistical noise in the SPIDER dataset, the modeling errors resulting from the approximations made in each result in a small, but non-negligible change in σ_r .

Template-based and harmonic domain methods make entirely different assumptions about the behavior of foregrounds. The value of employing multiple component separation pipelines lies in the capacity to explore the properties of foregrounds while evaluating the sensitivity of the result to different analysis choices. Future *B*-mode observational programs will need to carefully consider the impact of these modeling choices on the likelihood of the tensor-to-scalar ratio.

In Section 3, we analyze the spectral energy distribution of polarized diffuse Galactic dust emission using a template-based approach, showing variations between two selected half-regions. We find that the statistical significance is robust to the choice of the dust template, *Planck* 217 or 353 GHz, with confidence levels of 3.2σ and 3.9σ for β_d , respectively. Diffuse dust emission in the SPIDER region is not accurately modeled by a single scaling of a polarized dust template, α , over the entire region. Future CMB component separation analyses will need to accommodate the possibility of spatial variation in the SED of diffuse polarized dust, or quantify the impact of any simplifying approximations. If confirmed and interpreted as a spatial variation in the emissivity index, β_d , this would challenge our understanding of the polarized interstellar medium.

Within a subset of the SPIDER region, the joint *Planck* 217 and 353 GHz template analysis provides evidence of a departure from a simple modified blackbody spectral energy distribution at more than 3σ , under the assumption that the

⁵ <https://pysm3.readthedocs.io/en/latest/models.html#dust>

morphology of dust emission is consistent at all frequencies within each region. In the context of a single temperature modified black body considered here, a break in the spectral index would be required to accommodate this result.

In Section 4 it is shown that, averaged over the full region, the spectral energy distribution of polarized dust is consistent with that of a modified blackbody over the range of frequencies probed by SPIDER and *Planck* HFI. The data provide no significant evidence for variation of the emissivity index with angular scale. The spatial distribution of the emission is found to be consistent with a power law in angular multipole. Given that the highest signal-to-noise dust emission drives the result in the full region, this finding is consistent with the analysis of the sub-regions.

Component separation may be complicated by line-of-sight frequency decorrelation, such as may result from multiple dust clouds with differing SEDs and orientations in the same line of sight. In Section 5, we look for evidence of this effect in our region in locally isolated structures and a global rotation of dust angles with frequency. We do not find any evidence for this effect.

Looking forward, the addition of 280 GHz data from the second flight of SPIDER in 2022-23 will provide constraints on dust foregrounds in this region of sky that are both complementary to and independent of *Planck*, enabling further exploration of the topics considered here.

ACKNOWLEDGMENTS

SPIDER is supported in the U.S. by the National Aeronautics and Space Administration under grants NNX07AL64G, NNX12AE95G, NNX17AC55G, and 80NSSC21K1986 issued through the Science Mission Directorate, and by the National Science Foundation through PLR-1043515. Logistical support for the Antarctic deployment and operations was provided by the NSF through the U.S. Antarctic Program. Support in Canada is provided by the Natural Sciences and Engineering Research Council and the Canadian Space Agency. Support in Norway is provided by the Research Council of Norway. The Dunlap Institute is funded through an endowment established by the David Dunlap family and the University of Toronto. The Flatiron Institute is supported by the Simons Foundation. JEG acknowledges support from the Swedish Research Council (Reg. no. 2019-03959) and the Swedish National Space Agency (SNSA/Rymdstyrelsen). This work is in part funded by the European Union (ERC, CMBeam, 101040169). J.M.N. acknowledges support from the Research Corporation for Science Advancement. K.F. acknowledges support from DOE grant DE-SC0007859 at the University of Michigan. We also wish to acknowledge the generous support of the David and Lucile Packard Foundation, which has been crucial to the success of the project.

The collaboration is grateful to the British Antarctic Survey, particularly Sam Burrell, for invaluable assistance with data and payload recovery after the 2015 flight. We thank Brendan Crill and Tom Montroy for significant contributions to SPIDER’s development. Some of the results in this paper have been derived using the HEALPix package (Gorski et al. 2005). The computations described in this paper were performed on the GPC supercomputer at the SciNet HPC Consortium (Loken et al. 2010). SciNet is funded by the Canada Foundation for Innovation under the auspices of Compute Canada, the Government of Ontario, Ontario Research Fund - Research Excellence, and the University of Toronto.

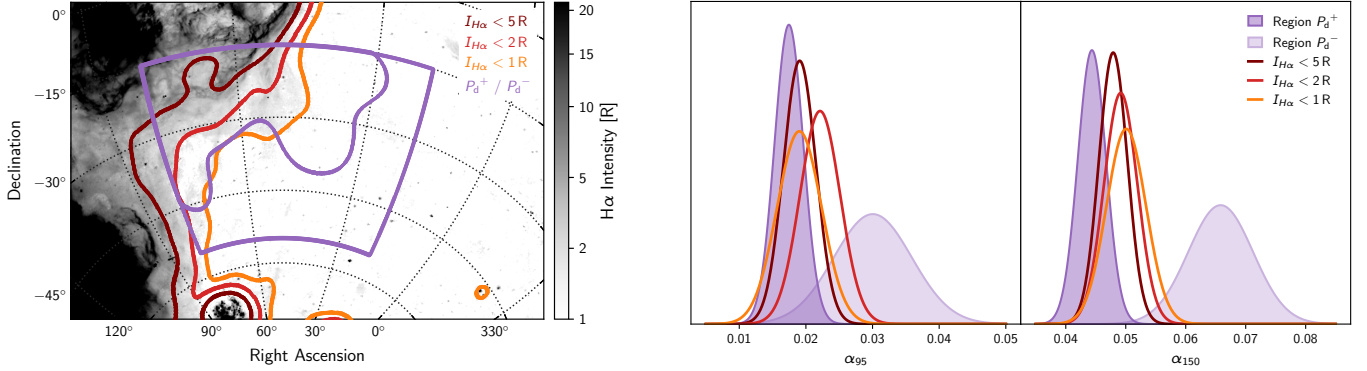


Figure 14. (left) The merged all-sky H α map from Finkbeiner (2003) in units of Rayleighs. The map is smoothed and thresholded at several intensities to create a series of masks (red/orange). The P_d^+ and P_d^- subregions of the SPIDER observing region are also overlaid (purple). (right) Plots of α_{95} and α_{150} 1-D likelihoods computed with the XFastest framework for the three Orion-Eridanus Superbubble masks, and compared to the likelihoods for the P_d^+ and P_d^- regions.

APPENDIX

A. IMPACT OF COMPACT STRUCTURES ON α_{150} SPATIAL VARIATION

In this Appendix, we assess the impact of the compact structures discussed in Section 3—the Orion-Eridanus Superbubble and the Magellanic Stream—on the detection of spatial variation in the value of α_{150} .

Following Soler et al. (2018), we use the full-sky H α map synthesized by Finkbeiner (2003) as a morphological tracer of the Orion-Eridanus Superbubble in the SPIDER region. In the background map of the left panel of Figure 14, the presence of the Orion-Eridanus Superbubble is evident in the top left corner of our region. To quantify its contribution to the determination of α_{150} , we mask the region it occupies with successively more aggressive thresholds. Specifically, for the reasons discussed in Section 3.1, we start by smoothing the Finkbeiner (2003) map with a 5 $^\circ$ -FWHM Gaussian. We then build three masks rejecting all pixels in which the H α emission is brighter than 5R (ayleighs), 2R, and 1R, respectively. The threshold-derived borders of these masks, which leave the SPIDER region with, respectively, 4.39%, 3.81%, and 3.06% of the sky, are shown in the left panel of Figure 14, along with the border of the P_d^+ and P_d^- subregions ($f_{\text{sky}} \approx 2.4\%$) used in the spatial variation analysis of Section 3. Finally, we compute α_{95} and α_{150} as in Section 3 using the *Planck* 353 GHz template, but for the full SPIDER region masked by each of the three H α masks. We chose the *Planck* 353 GHz template for this analysis because it provides the dominant contribution to the SMICA reconstructed dust map, as shown in Figure 1. Results from these subregions are shown in the right panel of Figure 14.

The value of α_{95} is quite robust to the choice of a Superbubble mask. In fact, the least aggressive mask results in the same value of α_{95} as the most aggressive mask, a value which remains consistent with that determined in the P_d^+ region. Similarly, although the value of α_{150} trends higher as we mask more aggressively—i.e., it trends towards its value in the P_d^- region—it remains largely consistent with its value in the P_d^+ region, with the P_d^+ and $I < 1R$ results in agreement at 1.4σ .

Therefore, the presence of the Orion-Eridanus Superbubble in the SPIDER region does not appear to drive the detected variation in the value of α_{150} .

The Magellanic Stream, which falls mostly outside of the SPIDER region aside from a few high-velocity clouds (HVCs) along the edge of its bottom right corner, also does not appear to be driving the detected spatial variation in the value of α_{150} . Indeed, none of the H α masks shown in Figure 14 exclude the HVCs. Nevertheless, the values of α_{150} derived in the full SPIDER region after application of any of these masks are consistent with each other, but inconsistent with those found in the P_d^- region, in which the HVCs also remain. If HVCs were the cause of the detected spatial variation in α_{150} , we would expect these four results to be in agreement.

B. CONVERSION BETWEEN TEMPLATE α AND SPECTRAL INDEX β

Galactic dust emission is modeled as a single MBB with a power-law emissivity,

$$I(\nu) = \tau_0 \left(\frac{\nu}{\nu_0} \right)^\beta B(\nu, T), \quad (\text{B1})$$

Table 2. Effective *Planck* and SPIDER band centers in GHz for different input SED models. Band center labels correspond to the CMB and dust models used throughout the main text.

SED Description	Label	<i>Planck</i>				SPIDER	
		100 GHz	143 GHz	217 GHz	353 GHz	95 GHz	150 GHz
Flat $I(\nu) = 1$	$\bar{\nu}^{\text{CMB}}$	101.2	142.6	221.4	360.6	94.8	150.8
$\alpha_{pl} = 4$		105.1	148.1	228.8	371.4	96.9	154.0
MBB ($\beta_d = 1.53, T_d = 19.6\text{K}$)	$\bar{\nu}^d$	104.5	147.2	227.3	368.8	96.6	153.5
MBB ($\beta_d = 1.59, T_d = 22.0\text{K}$)		104.5	147.3	227.5	369.1	96.6	153.5

where τ_0 is the optical depth at the reference frequency ν_0 . Throughout the text, we use β_d and T_d to refer to the spectral index and temperature of the dust component as defined in Equation B1. We calculate an effective observing frequency using the dust SED that takes into account the bandpass of the observing instrument. In general,

$$\bar{\nu} = \frac{\int d\nu \nu I(\nu) t(\nu)}{\int d\nu I(\nu) t(\nu)}, \quad (\text{B2})$$

where $I(\nu)$ is the SED of the observed source and $t(\nu)$ is the spectral transmission of the detector, properly normalized to its optical efficiency ϵ . This equation is a generalization of Equation 4 of [Planck Collaboration et al. \(2014\)](#). There, they express $I(\nu)$ for a power-law like SED: $I(\nu) \sim (\nu/\nu_0)^{\alpha_{pl}}$. Note that we identify the spectral index for this simple SED as α_{pl} to differentiate it from the template coefficients α_{95} and α_{150} used throughout the main text.

Table 2 lists effective frequency band centers for a variety of SED models. The results presented in [Planck Collaboration et al. \(2014\)](#) assume the $\alpha_{pl} = 4$ SED. However, this assumption holds true only in the Rayleigh-Jeans limit, and only when $\beta \approx 2$. A more accurate effective frequency can be calculated by considering the true dust SED.

CMB maps are typically shown in so-called thermodynamic units (μK_{CMB}), which encode the amplitude of fluctuations about the CMB temperature, $T_{\text{CMB}} = 2.725\text{K}$. The amplitude of dust emission can be expressed in these units by normalizing the dust emissivity with a first-order Taylor expansion of the CMB blackbody emission about $T = T_{\text{CMB}}$:

$$\Delta T(\bar{\nu}^d) = \left(\frac{\partial B}{\partial T} \Big|_{T=T_{\text{CMB}}} \right)^{-1} I(\bar{\nu}^d) = \frac{(e^x - 1)^2}{x^2 e^x} \frac{1}{2k} \left(\frac{c}{\bar{\nu}^{\text{CMB}}} \right)^2 I(\bar{\nu}^d). \quad (\text{B3})$$

Here, for convenience, we have defined $x \equiv h\bar{\nu}^{\text{CMB}}/(kT_{\text{CMB}})$. This equation describes the anisotropy in the mm-map caused by dust emission. It is important to note that the effective frequency used for conversion to thermodynamic units ($\bar{\nu}^{\text{CMB}}$) differs from the effective frequency used for the dust scaling ($\bar{\nu}^d$). The map-domain scaling relationship from a reference frequency ν_0 to a lower frequency ν is then expressed as

$$A(\bar{\nu}^d, \bar{\nu}_0^d; \beta_d, T_d) = \frac{\Delta T(\bar{\nu}^d)}{\Delta T(\bar{\nu}_0^d)} = \frac{(e^x - 1)^2}{x^2 e^x} \frac{x_0^2 e^{x_0}}{(e^{x_0} - 1)^2} \left(\frac{\bar{\nu}_0^{\text{CMB}}}{\bar{\nu}^{\text{CMB}}} \right)^2 \left(\frac{\bar{\nu}^d}{\bar{\nu}_0^d} \right)^{\beta_d} \frac{B(\bar{\nu}^d, T_d)}{B(\bar{\nu}_0^d, T_d)}. \quad (\text{B4})$$

Because we construct dust templates from *Planck* difference maps, specifically 353–100 GHz or 217–100 GHz, there is a minor subtraction of dust at 100 GHz. Consequently, the scaling of the difference template to a frequency ν is thus given by

$$\alpha(\bar{\nu}^d, \bar{\nu}_0^d; \beta_d, T_d) = \frac{\Delta T(\bar{\nu}^d)}{\Delta T(\bar{\nu}_0^d) - \Delta T(\bar{\nu}_{100}^d)} = \frac{A(\bar{\nu}^d, \bar{\nu}_0^d; \beta_d, T_d)}{1 - A(\bar{\nu}_{100}^d, \bar{\nu}_0^d; \beta_d, T_d)}, \quad (\text{B5})$$

where $\bar{\nu}_{100}^d = 104.5\text{GHz}$ according to Table 2. To recover a value of β_d given α , Equation B5 must be inverted using numerical methods.

C. COMPARISON TO ALL PYSM3 DUST MODELS

Section 6 and Figure 13 present a comparison between PySM3 dust models and the dust component estimated by SMICA. For simplicity, that comparison used only a representative subset of the available models. The remaining ones are shown in Figure 15.

Due to the fact that both the SPIDER SMICA results and the PySM3 models incorporate—to varying extents—both the *Planck* data and noise simulations, the covariance between them is non-trivial. While this makes a quantitative measure of the goodness

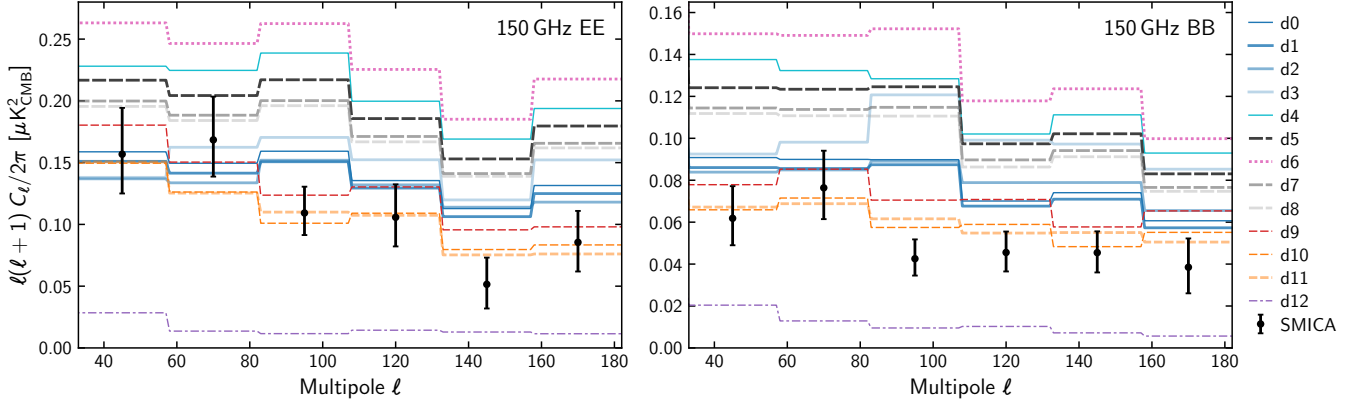


Figure 15. Companion to Figure 13 with the remaining PySM3 dust models. As before, this compares the *EE* (left) and *BB* (right) spectra from the PySM3 dust models (colored lines) to SMICA-derived dust bandpowers at 150 GHz (black points) in the SPIDER region. Models based on the same underlying inputs and class of SED modeling are shown with the same line style. Models drawn with thinner lines are those already shown in Figure 13.

of fit between the SPIDER data and the models difficult to assess, we reiterate that the overall amplitude of the SPIDER SMICA result is driven by the SPIDER 95 and 150 GHz data, and is therefore largely independent from the amplitude of the models shown. The amplitudes of the **d9–d11** family of models are in closest agreement with the SMICA amplitudes at 150 GHz. Most other models predict more power than SPIDER, except **d12**, which predicts significantly less.

For convenience, we provide a brief description of the PySM3 dust models shown in Figure 15. For a definitive description we refer the reader to the official documentation⁶.

Models d0–d4: This family of models treats thermal dust emission as a single-component modified black body (MBB). Polarized dust templates are based on the *Planck* 353 GHz channel, and are scaled to other frequencies using an MBB spectral energy distribution (SED). The polarization templates are smoothed with a Gaussian kernel of 2.6° FWHM, with power at smaller scales added according to the model described in the reference. For the SED, the models use:⁷

d0: A spatially fixed spectral index $\beta_d = 1.54$ and a black body temperature, $T_d = 20\text{K}$.

d1: A spatially varying spectral index and temperature based upon those provided in the *Planck* Commander maps (Planck Collaboration et al. 2016b), which assume the same spectral index for both intensity and polarization.

d2 (d3): An emissivity index that varies spatially on degree scales, drawn from a Gaussian with $\beta = 1.59 \pm 0.2$ (0.3).

d4: The two component (one hot, one cold) dust model of Finkbeiner et al. (1999).

Models d5, d7, d8: Implementations of the model described in Hensley & Draine (2017), using:

d5: The baseline model of that reference.

d7: A model including iron inclusions in the grain composition.

d8: A simplified version of **d7** in which the interstellar radiation field strength is uniform.

Model d6: A model that averages over spatially varying dust spectral indices, both unresolved and along the line of sight, using the frequency covariance of Vansyngel et al. (2017) to calculate the frequency dependence.

Models d9–d11: A family of models using a single component MBB with templates based on the *Planck* GNILC analysis (Planck Collaboration et al. 2020a), using the 353 GHz color correction described in (Planck Collaboration et al. 2020b). The frequency modeling uses:

d9: A fixed spectral index $\beta_d = 1.48$ and temperature $T_d = 19.6\text{K}$.

⁶ <https://pysm3.readthedocs.io/en/latest/models.html#dust>

⁷ Here we define families of models by their class designation within PySM3.

d10: Additional small scale fluctuations in the template, as well as the dust spectral index and temperature.

d11: Identical to **d10**, but using a different set of seeds and maximum multipole to generate the small scale features.

Model d12: A three-dimensional model of Galactic dust emission based on [Martínez-Solaéche et al. \(2018\)](#).

REFERENCES

- Abazajian, K. N., et al. 2016, arXiv:1610.02743
- Adam, R., Ade, P. A., Aghanim, N., et al. 2016, *Astronomy & Astrophysics*, 594, A10
- Balkenhol, L., Dutcher, D., Mancini, A. S., et al. 2023, *Physical Review D*, 108, 023510
- BICEP2/Keck, Planck Collaborations, Ade, P. A. R., Aghanim, N., et al. 2015, *Phys. Rev. Lett.*, 114, 101301. <https://link.aps.org/doi/10.1103/PhysRevLett.114.101301>
- BICEP/Keck Collaboration, Ade, P. A. R., Ahmed, Z., et al. 2021, *PhRvL*, 127, 151301
- . 2023, *ApJ*, 945, 72
- Brandt, W. N., Lawrence, C. R., Readhead, A. C. S., Pakianathan, J. N., & Fiola, T. M. 1994, *ApJ*, 424, 1
- Caldwell, R. R., Hirata, C., & Kamionkowski, M. 2017, *The Astrophysical Journal*, 839, 91. <https://dx.doi.org/10.3847/1538-4357/aa679c>
- Cardoso, J.-F., Le Jeune, M., Delabrouille, J., Betoule, M., & Patanchon, G. 2008, *IEEE Journal of Selected Topics in Signal Processing*, 2, 735
- Chon, G., Challinor, A., Prunet, S., Hivon, E., & Szapudi, I. 2004, *Monthly Notices of the Royal Astronomical Society*, 350, 914
- Clark, S., Kim, C.-G., Hill, J. C., & Hensley, B. S. 2021, *The Astrophysical Journal*, 919, 53
- Draine, B. T., & Fraise, A. A. 2009, *ApJ*, 696, 1
- Draine, B. T., & Li, A. 2007, *ApJ*, 657, 810
- Dunkley, J., Amblard, A., Baccigalupi, C., et al. 2009, in *American Institute of Physics Conference Series*, Vol. 1141, CMB Polarization Workshop: Theory and Foregrounds: CMBPol Mission Concept Study, ed. S. Dodelson, D. Baumann, A. Cooray, J. Dunkley, A. Fraise, M. G. Jackson, A. Kogut, L. Krauss, M. Zaldarriaga, & K. Smith, 222–264
- Finkbeiner, D. P. 2003, *The Astrophysical Journal Supplement Series*, 146, 407. <https://doi.org/10.1086%2F374411>
- Finkbeiner, D. P., Davis, M., & Schlegel, D. J. 1999, *The Astrophysical Journal*, 524, 867
- Galliano, F., Galametz, M., & Jones, A. P. 2018, *ARA&A*, 56, 673
- Gambrel, A. E., Rahlin, A. S., Song, X., et al. 2021, *ApJ*, 922, 132
- Gorski, K. M., Hivon, E., Banday, A., et al. 2005, *The Astrophysical Journal*, 622, 759
- Hazumi, M., Ade, P. A., Adler, A., et al. 2020, in *Space Telescopes and Instrumentation 2020: Optical, Infrared, and Millimeter Wave*, ed. M. Lystrup, N. Batalha, E. C. Tong, N. Siegler, & M. D. Perrin (SPIE). <http://dx.doi.org/10.1117/12.2563050>
- Hensley, B. S., & Bull, P. 2018, *ApJ*, 853, 127
- Hensley, B. S., & Draine, B. T. 2017, *The Astrophysical Journal*, 834, 134. <https://dx.doi.org/10.3847/1538-4357/834/2/134>
- Hensley, B. S., & Draine, B. T. 2022, arXiv e-prints, arXiv:2208.12365
- Hensley, B. S., Clark, S. E., Fanfani, V., et al. 2022, *The Astrophysical Journal*, 929, 166. <http://dx.doi.org/10.3847/1538-4357/ac5e36>
- HI4PI Collaboration, Ben Bekhti, N., Flöer, L., et al. 2016, *A&A*, 594, A116
- Hogg, D. W., Bovy, J., & Lang, D. 2010, arXiv e-prints, arXiv:1008.4686
- Huffenberger, K. M., Rotti, A., & Collins, D. C. 2020, *The Astrophysical Journal*, 899, 31. <https://dx.doi.org/10.3847/1538-4357/ab9df9>
- Hurier, G., Macías-Pérez, J. F., & Hildebrandt, S. 2013, *A&A*, 558, A118
- Kamionkowski, M., & Kovetz, E. D. 2016, *Annual Review of Astronomy and Astrophysics*, 54, 227. <https://doi.org/10.1146/annurev-astro-081915-023433>
- Kandel, D., Lazarian, A., & Pogosyan, D. 2017, *Monthly Notices of the Royal Astronomical Society: Letters*, 472, L10. <https://doi.org/10.1093/mnrasl/slx128>
- Leung, J. S.-Y., Hartley, J., Nagy, J. M., et al. 2022, *The Astrophysical Journal*, 928, 109. <http://dx.doi.org/10.3847/1538-4357/ac562f>
- Li, A., & Draine, B. T. 2001, *ApJ*, 554, 778
- Loken, C., Gruner, D., Groer, L., et al. 2010, in *Journal of Physics: Conference Series*, Vol. 256, IOP Publishing, 012026
- Martínez-Solaéche, G., Karakci, A., & Delabrouille, J. 2018, *Monthly Notices of the Royal Astronomical Society*, 476, 1310
- Mathewson, D. S., Cleary, M. N., & Murray, J. D. 1974, *ApJ*, 190, 291
- Page, L., Hinshaw, G., Komatsu, E., et al. 2007, *ApJS*, 170, 335
- Pelgrims, V., Clark, S. E., Hensley, B. S., et al. 2021, *A&A*, 647, A16
- Planck Collaboration. 2016, *Astronomy & Astrophysics*, 594, A10
- Planck Collaboration, Ade, P. A. R., Aghanim, N., et al. 2014, *A&A*, 571, A9
- Planck Collaboration, Adam, R., Ade, P. A. R., et al. 2016a, *A&A*, 586, A133
- . 2016b, *Astronomy & Astrophysics*, 594, A10

- Planck Collaboration, Akrami, Y., Ashdown, M., et al. 2020a, *A&A*, 641, A4
- . 2020b, *A&A*, 641, A11
- Planck Collaboration, Aghanim, N., Akrami, Y., et al. 2020c, *A&A*, 641, A3
- Planck Collaboration, Aghanim, N., Akrami, Y., et al. 2020d, *Astronomy & Astrophysics*, 641, A12.
<https://doi.org/10.1051/0004-6361/201833885>
- Plaszczynski, S., Montier, L., Levrier, F., & Tristram, M. 2014, *MNRAS*, 439, 4048
- Poh, J., & Dodelson, S. 2017, *Phys. Rev. D*, 95, 103511.
<https://link.aps.org/doi/10.1103/PhysRevD.95.103511>
- Purcell, E. M. 1975, in *The Dusty Universe*, ed. G. B. Field & A. G. W. Cameron, 155–167
- Remazeilles, M., Dickinson, C., Eriksen, H. K. K., & Wehus, I. K. 2016, *Monthly Notices of the Royal Astronomical Society*, 458, 2032. <https://doi.org/10.1093/mnras/stw441>
- Ritacco, A., Boulanger, F., Guillet, V., et al. 2023, *A&A*, 670, A163. <https://doi.org/10.1051/0004-6361/202244269>
- Seljak, U., & Zaldarriaga, M. 1997, *PhRvL*, 78, 2054
- Soler, J. D., Bracco, A., & Pon, A. 2018, *Astronomy & Astrophysics*, 609, L3.
<https://doi.org/10.1051%2F0004-6361%2F201732203>
- SPIDER Collaboration, Ade, A. R., Amiri, M., et al. 2022, *The Astrophysical Journal*, 927, 174.
<https://dx.doi.org/10.3847/1538-4357/ac20df>
- Tassis, K., & Pavlidou, V. 2015, *MNRAS*, 451, L90
- The Simons Observatory Collaboration, Ade, P., Aguirre, J., et al. 2019, *Journal of Cosmology and Astroparticle Physics*, 2019, 056
- Thorne, B., Dunkley, J., Alonso, D., & Naess, S. 2017, *Monthly Notices of the Royal Astronomical Society*, 469, 2821.
<http://dx.doi.org/10.1093/mnras/stx949>
- Vansyngel, F., Boulanger, F., Ghosh, T., et al. 2017, *A&A*, 603, A62
- Wright, E. L., Mather, J. C., Bennett, C. L., et al. 1991, *ApJ*, 381, 200